33

Basic Principles and Methodologies in Measuring Bone Biomechanics

Russell P. Main

CONTENTS

Introduction

The vertebrate skeleton serves many roles, including functional mechanical support and leverage for muscle action, a source for endocrine signals and a mineralized repository for assisting in ion homeostasis in the body. In extinct animals, for which we only have fossil remains, it is usually the mechanical functions of the bones and teeth that most capture our imagination and spark some of the greatest debate about species evolution, including the evolution of flight in birds and bipedal locomotion in primates. Similar functional debates date to some of the earliest examples of mineralized tissues in the fossil record, such as conodonts (Purnell 1993, Martínez-Pérez et al. 2014). Although the evolution of bizarre or unique bony structures has received considerable attention, these structures are often the most difficult to explain through defensible functional hypotheses. At the same time, an argument for the functional importance of highly conserved structures such as teeth, basic elements of the masticatory apparatus, and the proximal limb skeleton in sarcopterygians can be made given their conservation among a wide diversity of taxa. Furthermore, functional hypotheses for these conserved structures are less hampered by assumptions and better supported by phylogenetic analyses, which may include extant representatives with similar structures (Witmer 1995).

This chapter is focused on the multiscale mechanical forces experienced by the vertebrate skeleton. The specific objectives of this chapter are to discuss (1) the hierarchical organization of bone and the relevant mechanical forces experienced by the different skeletal components, (2) how skeletal function and its material properties are assessed experimentally, (3) the strengths and limitations in modeling skeletal mechanics, and (4) developing hypotheses and testing questions about skeletal biomechanics in extant and extinct species.

The Hierarchical Organization of Bone Tissue, and Solid and Fluid Mechanics in the Vertebrate Skeleton

When a limb bone is loaded during locomotion, when the dentary transmits the forces of masticatory muscles to food items or when a bovid horn sustains impact, stress develops in the bone and the bone tissue deforms. Compared to industrially manufactured structural materials such as steel, aluminum and glass, bone is incredibly heterogeneous in its composition and structure. This heterogeneity, in part, allows bone to sustain relatively high forces (e.g., strength) and to absorb a high amount of load energy (e.g., toughness) without fracturing (Figure 33.1). At the nanoscale, bone tissue matrix is a mineral-protein composite of (typically) aligned, amorphous, hydroxyapatite mineral and type I collagen. Many other proteins are present as well and are important for type I collagen fibrillogenesis, the cross-linking of collagen molecules and the mineralization of collagen (Burr and Akkus 2014). Interrupting the continuity of this tissue matrix are the osteocytes, bone cells embedded in the tissue matrix, which are present over a large range of densities (8000–79,000 cells/cm^3) that vary across bone elements, locations in the bone and phylogeny (Qiu et al. 2002, D'Emic and Benson 2013, Stein and Werner 2013, Buenzli and Sims 2015).

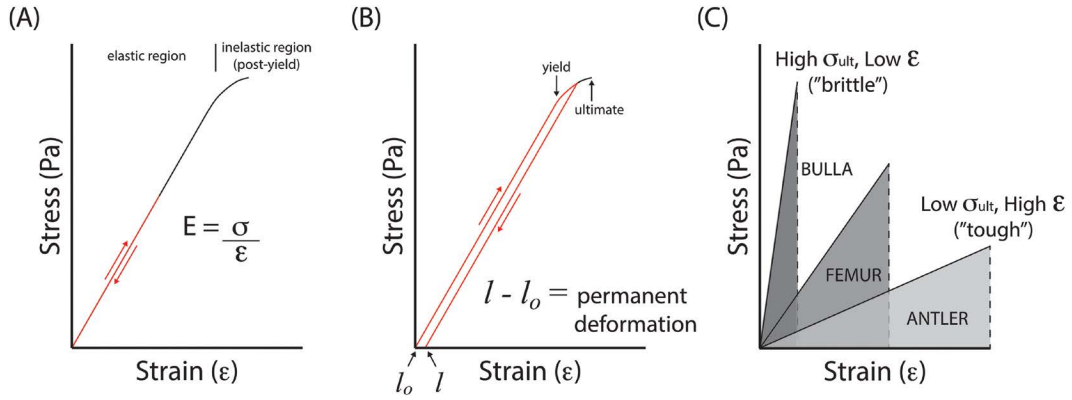

FIGURE 33.1 Stress-strain relationships for elastic and plastic deformation of a solid material (bone) with examples from different mammalian tissues. A, Elastic loading and unloading of tissue. B, Plastic deformation with loading beyond the linear elastic region. C, Examples of tissues with high mineral density (bulla) and low mineral density (antler). In (A), the material is loaded under increasing stress (σ) and strain (ε) before load is released and stress and strain return to zero. The relationship between applied stress and the resulting strain for linearly elastic materials is called the elastic (Young's) modulus (*E*). In (B), the material is loaded beyond the elastic limit, called the yield point, resulting in permanent deformation in the bone. When the load is released, the tissue stress returns to zero, but a permanent deformation remains ($l - l_o$). The unloading slope parallels the load slope. The bone sample would completely fracture on reaching the ultimate stress (or strain). In (C), the stress-strain curves for the whale bulla, deer antler and cow femur are presented. The bulla acts similar to a brittle material, like glass or ceramic, reaching a high ultimate stress (σ_{ult}) and absorbing little energy (area under the stress-strain curve) before fracturing. The antler is a tough material and absorbs more energy than the bulla or femur before breaking. (See Currey 1979 for more discussion.)

Many teleost fishes do not possess these cells. At a higher scale, the bone-cellular matrix is interrupted by vascular channels of varying density and organization (longitudinal, oblique, radial and circumferential vessels). Similar to engineered materials that bear load, bone is constantly experiencing dynamically changing loads that can cause fatigue damage to the bone tissue. However, unlike engineered materials that are devoid of living cells, this damage is constantly being remodeled by osteocytes, osteoclasts and osteoblasts to repair fatigue microdamage and, hypothetically, to align the mineral and collagen matrix with the prevailing loading conditions. The structural and histological consequence of this remodeling are secondary (Haversian) osteons. The bones of small animals and those with relatively thin cortices (e.g., birds, bats, small rodents) do not typically undergo intracortical remodeling, which places a greater importance on natural selection and adaptive plastic mechanisms for arriving at a viable bone morphology in these taxa.

All of these anatomical features contribute to what are defined as tissue-level material properties, such as bone mineral density (BMD, mg cm^{-3}) and elastic modulus. BMD is the density of the hydroxyapatite mineral present within a volume of bone tissue. With most radiation-based measurement tools (computed tomography [CT], X-ray), where the image resolution is greater than ~4 μm, this value also includes the lacunar-canalicular porosities, vascular pores and remodeling-induced resorption spaces. Micro-CT, nano-CT and synchrotron-based imaging modalities can identify some of these porosities, depending on the scan resolution. BMD relates directly to tissue elastic modulus (Carter and Hayes 1976, Currey 1999, Easley et al. 2010). Most of the experimentally determined values for elastic modulus have been derived from human bones or the bones of domesticated mammals (Table 33.1) (Currey 2002). The elastic modulus defines the physical relationship between stress and strain in the bone tissue. Stress is a normalized expression of force (axial tension or compression, bending or torque) relative to its distribution through an area of bone tissue, and strain is the resulting deformation of bone tissue in response to the applied stress (Figure 33.1A). In bone, the relationship between stress and strain is generally linear, until the yield point of the tissue is reached (Figure 33.1B). Within this region, the application of load (stress) will cause deformation as described by the linear relationship. As load is released, stress and strain (deformation) will decrease toward zero along this same relationship (Figure 33.1A). If a bone is loaded beyond its elastic region, surpassing the material yield point, induction of damage in the tissue will cause it to be permanently deformed on release of the load (Figure 33.1B). Permanent deformation is undesirable, and bone remodeling and adaptive modeling prevent it at the microstructural and gross levels. Loading beyond this yield point can cause the continued accumulation of damage in the tissue, which ultimately manifests as gross skeletal fracture.

While elastic modulus varies throughout the bone with local differences in BMD, it also varies across different anatomical axes. Anisotropy in tissue stiffness across different axes is due to differences in mineral, collagen and anatomical structure alignment across these axes. In long bones, the tissue is typically stiffest and strongest along the bone's long axis, coinciding with the predominant alignment of mineral and collagen along that axis. Cortical long bone tissue has been characterized as more compliant and weaker when tested in the radial and circumferential directions, where the radial direction is perpendicular to the periosteal and endosteal surfaces and the circumferential direction lies parallel to these surfaces. The bone is weaker in these directions because the applied forces can more easily separate crystals and collagen perpendicular to their long axes and across longitudinal vascular canals (Table 33.1) (Wainwright et al. 1982). Generally, bone is defined as transversely isotropic, maintaining similar mechanical characteristics across two axes, and possessing a third axis that differs from the other two (Bartel et al. 2006). Although the axial moduli are similar when

TABLE 33.1

Elastic Moduli (GPa), Ultimate Strength (MPa), and Ultimate Strain (ε) for Adult Mammalian Cortical Bone

	Human		Bovine		
	Haversian		Haversian		Fibrolamellar
	Tension	Compression	Tension	Compression	Tension
Elastic Modulus					
E_3	17.7	18.2	23.1	22.3	26.5
$E_1 = E_2$	12.8	11.7	10.4	10.1	11.0
G	3.3		3.6		5.1
Ultimate Strength					
σ_3	133	205	150	272	167
σ_1	53	131	54	171	55
σ_2	53	131	39	190	30
τ	67		70		64
Ultimate Strain					
ε_3	0.031	0.019	0.020	0.016	0.033
ε_1	0.007	0.050	0.007	0.042	0.007
ε_2	0.007	0.050	0.007	0.072	0.002
γ^v	0.0087				

Notes: 1, 2, 3 = circumferential, radial, longitudinal.

$\sigma_1 = \sigma_2$ assumed for humans; $E_1 = E_2$ assumed for humans and bovine samples.

γ^v, shear yield strain is presented because no published values for ultimate torsional strain could be found.

A valuable summary of these values can be found in Tables 3.1 and 3.2 in Currey (2002). Values for a comparative list of samples for some of these properties are provided in table 4.3 in Currey (2002). A useful review of the relationships between these properties and bone material properties, in general, can be found in the appendices of Carter and Beaupré (2001).

Source: Values taken from Reilly et al. (1974), Reilly and Burstein (1975), and Mirzaali et al. (2016).

tested under tension or compression, the bone tissue is stronger in compression, and this depends on differences in bone fracture mechanics in tension versus compression (Currey 2002).

One final basic property of bone and other materials is Poisson's ratio, which defines the deformation across two material axes on loading in the third axis. This effect is common in all solids and describes how contraction (or expansion) can occur in two axes on the application of tension (or compression) in the third axis. A value of 0.3–0.4 is typically assigned to bone (Carter and Beaupré 2001).

Tissue-level properties are important for determining the strength and stiffness of a whole bone, and so is the structural distribution of that tissue. Important structural properties of bone tissue include the cross-sectional area (A, mm^2) and the second and polar moments of area (I and J, respectively, mm^4). In cancellous bone tissue, properties such as bone volume fraction (%), trabecular thickness (mm), trabecular number (1/mm), connectivity (1/mm^3), degree of anisotropy and structure model index (SMI) have been used to describe the mechanical competence (Bouxsein et al. 2010). For an axial load applied at the end of a long bone, the axial stress (σ_{ax}) that the load imparts is positively related to the magnitude of the applied force (F) and negatively related to the cross-sectional area over which that force is distributed (Figure 33.2A). Bending loads occur in bone due to off-axis load components directed perpendicular to the bone's long axis and/or bending loads that develop under the application of axial loads, due to bone curvature (Biewener 1983a, b, Bertram and Biewener 1988) (Figure 33.2B, C). These bending stresses (σ_b) are directly related to the magnitude of the bending moment applied to the bone ($F \times d$), where d is the moment arm of the applied force, or the distance between the point of load application and the location at which σ_b is calculated. Under pure bending loads, compressive stresses ($-\sigma_b$) develop in half of the bone's cortex and tensile stresses ($+\sigma_b$) in the other half. Bending stresses decrease toward the center of the bone, where there is a neutral axis of zero stress, and increases the greater the distance (y) from the neutral axis (Figure 33.2B). Bending stresses are resisted by increased second moments of area for a bone cross-section. The second moment of area describes the distribution of bone tissue about a given anatomical axis. The more bone tissue (A) distributed further away from the bending axis of interest (y), the greater the value is for I (Figure 33.3A), and the lower the induced stresses for a given applied bending moment. In the case of the cross-section of the goat radius, Iyy, which resists mediolateral bending, is three times greater than is Ixx, which resists craniocaudal bending (Figure 33.3B). The predominance of bone loading in bending and torsion among tetrapods may be one factor contributing to hollow bone centers, where stresses are very low (Figure 33.3C).

As the limb mechanics of a more diverse array of tetrapod taxa have been sampled, torsional loads have been described as the dominant loading mode in the long bones of salamanders, lizards, turtles, alligators, the forelimb and hindlimb bones of birds, and some mammals with less purely parasagittal gaits (Table 33.2) (Biewener and Dial 1995, Blob and Biewener 1999, Carrano and Biewener 1999, Main and Biewener 2007, Butcher et al. 2008, 2011, Sheffield and Blob 2011, Sheffield et al. 2011, Kawano et al. 2016). Torsional loads are applied about a bone's long axis and act to twist the bone, inducing shear stress (τ) and strain (γ) in the bone tissue. Governing the relationship

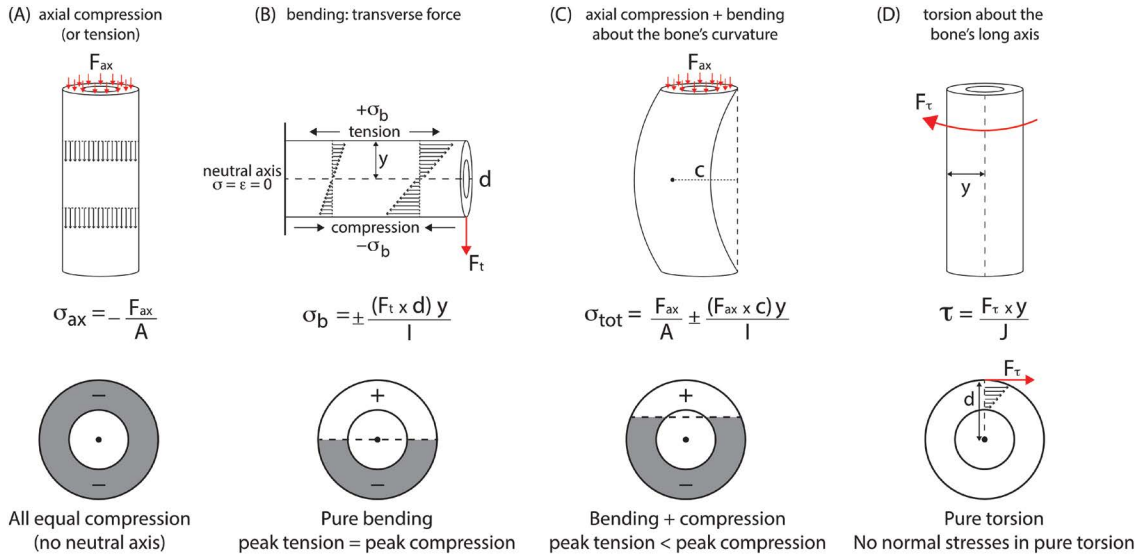

FIGURE 33.2 Different idealized loading modes for bone. A, A bone loaded in axial compression (F_{ax}) across its cross-sectional area (A). By definition, compressive stresses and strains are negative. Axial compression creates a uniform state of stress and strain within the tissue. The strain that develops from an applied stress depends on the elastic modulus for the material. Test bone samples loaded in the laboratory are often loaded in uniform axial tension or compression. B, A bone sample loaded in cantilever bending, as shown here, develops positive and negative stress ($+\sigma_b$, $-\sigma_b$) and strain that are uniform in pure bending. Stress and strain increase away from the neutral axis of bending to reach a maximum value at the bone sample's surface (y). The applied stress and strain are maximal at the end of the tissue (d) where the force (F_t) is applied and decreases toward the base ($d = 0$). Bending stress is countered by the distribution of bone tissue (second moment of area, I) around the bending axis. C, A sample is loaded in axial compression about the bone's radius of curvature (c). Both axial compression and bending stresses and strains develop in the bone. The convex surface experiences tension, as in pure bending, but this is overlain by axial compression, which shifts the neutral axis toward the convex surface. Both A and I are important in resisting these loads, meaning that the material area as well as its distribution about the axis of bending are important. D, A bone loaded in torsion about the bone's long axis. Torsional shear stresses (τ) increase with distance (y) from the centroid. Torsional loads are resisted by the polar moment of inertia (J), which is maximized when $I_{MAX} = I_{MIN}$ (e.g., circle).

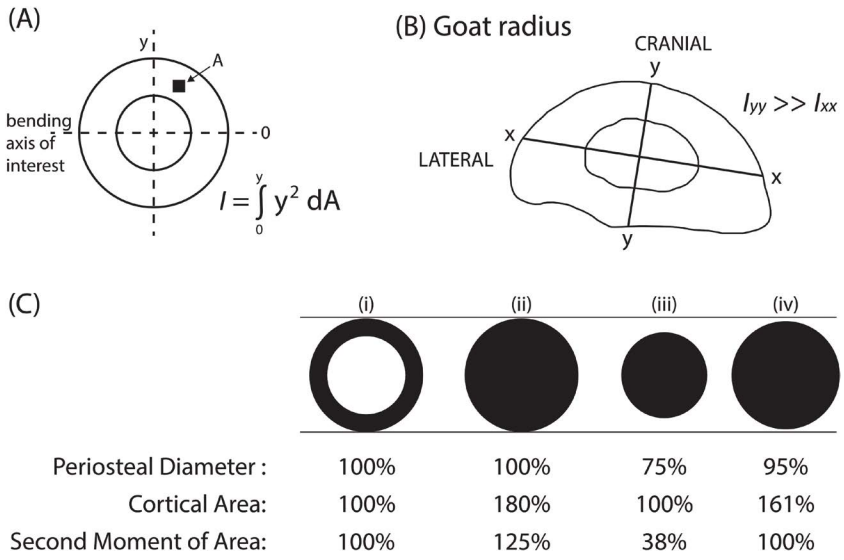

FIGURE 33.3 Second moment of area in resisting bending and torsional loads. A, The second moment of area (I, also called the moment of inertia) is highly influenced by the squared distance of each measurable bone unit away from the neutral axis (y^2). The more bone located at a distance from the neutral axis, the more resistant the structure is to bending (though local buckling may still be a concern) (Currey 2002). B, A transverse cross-section of the goat radius where I_{yy} ($= I_{MAX}$) and I_{xx} ($= I_{MIN}$) are based on structure alone, without information about *in vivo* bending regimes in the bone. In this case, I_{yy} is much greater than I_{xx}, suggesting greater resistance to mediolateral bending in an animal that swings its leg in a craniocaudal (parasagittal) direction. The selective forces shaping this bone may be constraining this bone's shape for the sake of load predictability, rather than minimizing craniocaudal stresses and strains (Bertram and Biewener 1988, Main and Biewener 2004). C, Relationships among periosteal diameter, cortical area, and the second moment of area. A wide, hollow bone maximizes both I and J, while minimizing weight (e.g., cortical area). Solid bones (ii, iv) that outperform or are similar to (i) in terms of I, are much heavier ($\gg A$), while solid bones with as much mass as (i) are much less resistant to bending and torsional loads (iii). (Based on van der Meulen et al. 2001.)

TABLE 33.2

In Vivo Long Bone and Cranial Bone Strains Collected Using Axial or Rosette Strain Gauges*

Genus	Species	Bone Measured	Peak Principal (or Axial) Strain (με)	Peak Shear Strain (με)	Activity	Reference
LONG BONES						
Amphibia						
Lithobates	*catesbeiana*	Femur	470	475	Hopping	Blob et al. (2014)
Chaunus	*marinus*	Femur	208[a]		Hopping	Blob et al. (2014)
Reptilia (Including Aves)						
Pseudemys	*concinna*	Humerus	1398[a]	730	Walking	Young et al. (2017)
		Femur	–1701	2934	Walking	Butcher et al. (2008)
Trachemys	*scripta*	Femur	2000	1446	Walking	Young and Blob (2015)
Iguana	*iguana*	Femur	629	1121	Running	Blob and Biewener (1999)
		Tibia	1650[a]		Running	Blob and Biewener (1999)
Tupinambis	*merinae*	Femur	–238	278	Walking	Sheffield et al. (2011)
Alligator	*mississippiensis*	Humerus	–416	520	Walking	Blob et al. (2014)
		Femur	708	1027	Walking	Blob and Biewener (1999)
		Tibia	–880[a]	677	Walking	Blob and Biewener (1999)
Dromaius	*novaehollandiae*	Femur	1749	3405	Running	Main and Biewener (2007)
		Tibiotarsus	–1863	3583	Running	Main and Biewener (2007)
Gallus	*gallus*	Femur	856	224	Walking	Carrano and Biewener (1999)
		Tarsometatarsus	–900[a]	800	Walking	Loitz and Zernicke (1992)
		Tibiotarsus	–1870		Running	Biewener et al. (1986)
		Ulna	–2100		Flapping	Rubin and Lanyon (1982)
Meleagris	*gallopavo*	Tibiotarsus	–2350		Running	Rubin and Lanyon (1984a)
		Ulna	–1900		Flapping	Rubin and Lanyon (1984b), Fritton et al. (2000)
Anser	sp.	Humerus	–2800		Flying	Rubin and Lanyon (1984a)
Columba	*livia*	Humerus	–2330	1780	Vertical flight/level flight	Biewener and Dial (1995)
Mammalia						
Potoroo	*tridactylus*	Calcaneus	–1200		Hopping	Biewener et al. (1996)
Didelphis	*virginiana*	Femur	–713[a]	419	Running	Butcher et al. (2011)
Dasypus	*novemcinctus*	Femur	1226[a]	464	Running	Copploe et al. (2015)
Equus	*caballus*	Metacarpus	–1900		Trotting	Gross et al. (1992)
		Metacarpus	–4840		Galloping	Nunamaker et al. (1990)
		Metacarpus	–2430		Jumping	Biewener (1993)
		Metacarpus	–3000		Accelerating	Biewener (1993)
		Metatarsus	–1710		Galloping	Biewener (1993)
		Metatarsus	–4005		Jumping	Biewener (1993)
		Radius	–2800		Galloping	Rubin and Lanyon (1982)
		Radius	–3690		Jumping	Biewener (1993)
		Tibia	–3170		Galloping	Rubin and Lanyon (1982)
		Tibia	–5180		Jumping	Biewener (1993)
Ovis	*aries*	Calcaneus	–328	534	Trotting	Lanyon (1973)
		Femur	–700		Walking	Lanyon et al. (1981)
		Metatarsal	–1291		Trotting	Lieberman et al. (2004b)
		Radius	–1764		Walk	Lanyon et al. (1979)
		Tibia	–759		Trotting	Lieberman et al. (2004b)
		Tibia	–2100		Trotting	Lanyon and Bourn (1979)
		Vertebrae	270[a]		Trotting	Lanyon (1972)
Capra	*hircus*	Metacarpus (juvenile)	–1324[a]		Galloping	Moreno et al. (2008)
		Radius	–1850		Galloping	Biewener and Taylor (1986)
		Tibia	–1970		Galloping	Biewener and Taylor (1986)
Sus	*scrofa*	Radius	–2400		Trotting	Goodship et al. (1979)
Canis	*lupus*	Femur	–460		Walking	Manley et al. (1982)

TABLE 33.2 (Continued)

Genus	Species	Bone Measured	Peak Principal (or Axial) Strain (με)	Peak Shear Strain (με)	Activity	Reference
		Radius	–2600		Galloping	Rubin and Lanyon (1982)
		Radius	400[a]	650	Walking	Carter et al. 1980
		Tibia	–2020		Galloping	Rubin and Lanyon (1982)
		Ulna	780[a]	740	Walking	Carter et al. (1980)
Mus	*musculus*	Tibia	600[a]		Walking	Sugiyama et al. (2012)
		Ulna	1676[a]		Trotting	Lee et al. (2002)
Rattus	*norvegicus*	Femur	–410	375	Walking	Keller and Spengler (1982, 1989)
		Tibia	740[a]		Walking	Rabkin et al. (2001)
		Ulna	–1200[a]		Running	Mosley et al. (1997)
Pteropus	*poliocephalus*	Humerus	–2004		Flying	Swartz et al. (1992)
		Radius	–2184		Flying	Swartz et al. (1992)
Hylobates	*lar*	Humerus	1492		Brachiating	Swartz et al. (1989)
		Radius	–1638		Brachiating	Swartz et al. (1989)
		Ulna	1421		Brachiating	Swartz et al. (1989)
Macaca	*mulatta*	Tibia	1272		Galloping	Demes et al. (2001)
		Ulna	1099		Galloping	Demes et al. (1998)
Homo	*sapiens*	Femur	1340		One-legged stand	Aamodt et al. (1997)
		Tibia	1675	5027	Running (17 km/h)	Milgrom et al. (2000)
CRANIAL BONES						
Osteichthyes						
Lepomis	*macrochirus*	Opercular	–1800		Prey strike	Lauder and Lanyon (1980)
Polypterus	*endlicheri*	Frontal	–174		Suction of prey	Markey et al. (2006)
Reptilia						
Anolis	*equestris*	Frontal	–1195	2036	Biting	Ross et al. (2018)
Gekko	*gekko*	Frontal	940	1774	Biting	Ross et al. (2018)
Iguana	*iguana*	Frontal	517	1008	Biting	Ross et al. (2018)
Uromastyx	*geyri*	Jugal	–1936	3195	Biting	Porro et al. (2014)
Salvator	*merianae*	Frontal	1004	1256	Biting	Ross et al. (2018)
Varanus	*exanthematicus*	Frontal	2000		Biting	Smith and Hylander (1985)
Alligator	*mississippiensis*	Angular	–273	430	Biting	Porro et al. (2013), Ross and Metzger (2004)
		Anterior root of zygoma		2316	Biting	Ross and Metzger (2004)
		Dentary	–2757	3683	Biting	Porro et al. (2013), Ross and Metzger (2004)
		Frontal	942	1269	Biting	Metzger et al. (2005)
		Jugal	–2286	3653	Biting	Metzger et al. (2005)
		Maxilla	2032	3943	Biting	Metzger et al. (2005)
		Prefrontal	–2085	3833	Biting	Metzger et al. (2005)
		Quadrate		644	Biting	Ross and Metzger (2004)
		Splenial	–2500	1373	Biting	Porro et al. (2013)
		Surangular		2162	Biting	Ross and Metzger (2004)
Mammalia						
Ovis	*aries*	Frontal	711	984	Chewing	Thomason et al. (2001)
Sus	*scrofa*	Frontal	136	76	Chewing	Sun et al. (2004), Ross and Metzger (2004)
		Mandible		213	Chewing	Ross and Metzger (2004)
		Maxilla		379	Chewing	Ross and Metzger (2004)
		Nasal		67	Chewing	Ross and Metzger (2004)
		Parietal	89	65	Chewing	Herring and Teng, (2000), Ross and Metzger (2004)
		Premaxilla		130	Chewing	Ross and Metzger (2004)
		Squamosal	984	1303	Chewing	Rafferty et al. (2000)

(Continued)

TABLE 33.2 (Continued)

Genus	Species	Bone Measured	Peak Principal (or Axial) Strain (με)	Peak Shear Strain (με)	Activity	Reference
		Zygomatic	891	1729	Chewing	Rafferty et al. (2000), Herring et al. (2005)
Oryctolagus	*cuniculus*	Mandible	320		Chewing	Weijs and de Jongh (1977)
Procavia	*capensis*	Frontal	273	432	Chewing	Lieberman et al. (2004a)
		Mandible	–757	1093	Chewing	Lieberman et al. (2004a)
		Nasal	–113	156	Chewing	Lieberman et al. (2004a)
		Zygomatic arch	891	1729	Chewing	Lieberman et al. (2004a)
Macaca	*mulatta*	Mandible	–981	1941	Biting	Hylander and Bays (1979), Ross (2001)
		Orbital roof	54	111	Biting	Ross (2001), Ross and Metzger (2004)
		Orbital wall	95	265	Biting	Ross (2001)
		Zygomatic arch	169	1194	Biting	Ross (2001)
M.	*fascicularis*	Frontal	292	411	Biting	Hylander et al. (1991a, b)
		Mandible	–894	1602	Biting	Hylander (1979)
		Zygomatic arch	–1262	1970	Biting	Hylander and Johnson (1997)
Macaca	sp.	Postorbital bar		188	Chewing	Ross and Metzger (2004)
		Postorbital septum		48	Chewing	Ross and Metzger (2004)
Aotus	sp.	Mandible		1090	Biting	Ross (2001)
		Medial orbital wall		188	Biting	Ross (2001), Ross and Metzger (2004)
A.	*trivirgatus*	Frontal	–177	313	Chewing	Ross and Hylander (1996)
		Postorbital bar	690	532	Chewing	Ross and Hylander (1996), Ross and Metzger (2004)
		Postorbital septum	300	210	Chewing	Ross and Hylander (1996), Ross and Metzger (2004)
Otolemur	*garnetti*	Frontal	–383	745	Chewing	Ravosa et al. (2000a, b)
O.	*crassicaudatus*	Frontal	–315	642	Chewing	Ravosa et al. (2000a, b)
		Mandible	–1149	2004	Biting	Hylander (1979)
Otolemur	sp.	Mandible		1301	Chewing	Ross and Metzger (2004)
		Postorbital bar		398	Chewing	Ross and Metzger (2004)
		Medial orbital wall		346	Chewing	Ross and Metzger (2004)
Eulemur	sp.	Dorsal orbital		109	Chewing	Ross and Metzger (2004)
		Frontal	123	100	Chewing	Ross and Metzger (2004)
		Mandible		600	Chewing	Ross and Metzger (2004)
		Postorbital bar	464	284	Chewing	Ross and Metzger (2004)
		Zygomatic arch		530	Chewing	Ross and Metzger (2004)
Sapajus	sp.	Mandible	1272		Biting	Ross et al. (2016)
Papio	*anubis*	Frontal	167	212	Chewing	Hylander et al. (1991a, b)

Notes: [a] Indicates axial data collected using a single element strain gauge. All other strains presented are principal strains or shear strains derived from rosette strain gauges.

Many bone locations and different surfaces on a single bone have been sampled for some species. For each bone, the greatest mean peak strains recorded are presented (e.g., peak strains averaged over multiple individuals), regardless of which surface that principal or shear strain data may have originated. In some cases, peak principal and peak shear strains may have originated on different surfaces on the same bone.

[*] It is interesting to note that for the long bone data, all major vertebrate groups are represented, except fish. For the cranial bone strains, both reptiles and primates are well represented, and there are even some fish. However, no bone strains have ever been recorded from a bird skull *in vivo*. While 22 species have been added since the last comprehensive list of *in vivo* strain data (Fritton and Rubin 2001), there are some key groups that are in desperate need of greater sampling for both long bone and cranial bone strains.

between torsion-induced shear stress and strain is the shear modulus (G). Like bending stresses, torsional stresses are positively related to the torsional moment applied to the bone ($\tau = F \times y$), where y is the distance of the applied force from the axis of rotation (Figure 33.2D). The axis of rotation in the analysis of long bone cortical biomechanics is the centroid. The peak torsional moment is resisted by the polar moment of inertia (J), calculated as the sum of the maximum and minimum second moments of area (I_{MAX}, I_{MIN}). As for bending stresses, the more bone tissue that is located further from the axis of rotation, the greater is the value of J, and the lower the torsional stresses and strains.

For a bone loaded in a combination of bending and axial compression or tension (Figure 33.2C), tissue-level stresses are distributed asymmetrically throughout the bone's cross-section, creating a stress or strain gradient in the direction of bending, with strain increasing from the medullary canal toward the periosteal bone surface (Figure 33.2C). It is important to note that the axis of bending during any activity (chewing, running, flying or swimming) can be constantly changing throughout the duty cycle, so a constant direction of bending in a bone should not be assumed (Rubin and Lanyon 1985, Blob and Biewener 1999, Main and Biewener 2004, 2006, Butcher et al. 2008). At the level of the living cells in the matrix, it is hypothesized that the strain gradients drive extracellular fluid through the osteocyte lacunar-canalicular system (OLCS). This fluid flow induces shear-based stress on the cell surface as well as drag-based stresses on the proteins in the glycocalyx anchoring the osteocytes and their processes to the boney matrix (Cowin et al. 1995, You et al. 2001, Wang et al. 2008, Fritton and Weinbaum 2009). Displacement of these tethering elements is transmitted to the cellular cytoskeleton by cell membrane integrins. Cytoskeletal deformation triggers physiological responses in the cell, stimulating anabolic bone signals to induce adaptive modeling in the loaded tissue, different from the signals that remove bone microdamage.

A high number of low-magnitude load cycles or a low number of high-magnitude load cycles (and combinations along this spectrum) can cause microcracks in the hydroxyapatite-collagen matrix that can coalesce into macroscopic cracks that may compromise the stiffness of the bone. Unlike acellular engineered materials, bone and other living tissues can dynamically repair this microscopic damage. These remodeling events are initiated, at least in part, by damage to the OLCS that results in the cellular production of proosteoclastic and provasculogenic factors (*RANKL*, *VEGF*) secreted by dying osteocytes near the crack (Burr et al. 1985, Kennedy et al. 2012). The results of these repair processes are the formation of secondary osteons in cortical tissues and hemiosteons in cancellous tissues. Once formed, the cement lines of secondary osteons can act as future growth arrestors that absorb crack elongation energy to blunt the progress of crack propagation during future loading events (Wainwright et al. 1982). The interface between the hydroxyapatite mineral and organic collagen phases in primary and secondary bone tissues have been hypothesized to act similarly. Primary bone is stiffer than completely remodeled bone in axial loading (Table 33.1) (Currey 2002) and has a fatigue life that is five times greater than secondary bone (Carter et al. 1976). The decrease in material properties that result from intracortical remodeling reflects the strength of selection on cellular mechanisms that remove microdamage in bone.

Measuring and Modeling *In Vivo* Skeletal Mechanics and Bone Tissue Properties

The best way to assess skeletal loading *in vivo* is to directly measure the tissue-level results of mechanical loading by surgically implanted strain gauges. However, this is not always possible to do even in extant taxa for a number of reasons, including ethical and practical concerns of working with humans or wild-caught animals, the minimum bone element size required for gauge implantation, and potentially poor locomotor or masticatory performance in a lab-based setting. When direct measures cannot be made, simplifying assumptions must be applied to estimate bone stress and strain using simple or computational models (Biewener 1983b, Rayfield 2007, Dumont et al. 2009, O'Higgins et al. 2012). There are also potential limitations in lab-based settings for locomotor studies because animals cannot typically achieve the entire range of behaviors in the lab that they would in the wild. Therefore, lab-based studies, although relatively easy to control for repeatable results, may not provide complete insight into the mechanical basis for the evolution of particular bone shapes and microstructures relative to *in vivo* mechanics in the wild.

Skeletal loading environments can be directly measured using implantable foil strain gauges. These strain gauges can be attached surgically to bone using self-catalyzing cyanoacrylate adhesive. *In vivo* strains from a wide variety of vertebrate taxa performing a vast array of locomotor and masticatory activities have been collected (Table 33.2). Rosette strain gauges are particularly helpful for determining principal strains at the measured location and the orientation of these strains relative to an anatomical axis of interest. Measures of shear strain induced by either eccentric or torsional bone loading may also be calculated from rosette strain gauges using standard equations (Carter et al. 1980, Biewener 1992, Biewener and Dial 1995, Carrano and Biewener 1999). One limitation of implantable strain gauges is that they only characterize strain at a single bone location that may not coincide with the location of peak strain in the bone. For long bones, it is generally difficult to assess how a bone is loaded without placing at least three rosette strain gauges around the circumference of the bone at the same anatomical level (e.g., mid-diaphysis). If this configuration is possible in the taxon of interest, rosette gauges will provide the direction of the principal and shear strains around the bone, while the longitudinal gauge readings can provide a cross-sectional analysis of the longitudinal distribution of normal strains at the anatomical location of gauge placement (Figure 33.4) (Biewener 1992).

Strain gauge analyses can be combined with kinematic, electromyographic (EMG) and/or force plate analyses to understand the contributions of limb positioning, muscle forces and ground reaction forces on local bone biomechanics (Reilly et al. 2005, Aiello et al. 2013). Strain gauge measures can be used as validation points for computational analyses, enabling the model to, with some confidence, project beyond the strict location of the gauges to other bony regions, such as cancellous bone tissues or the metaphysis (Porro et al. 2013, Yang et al. 2014, 2019, Panagiotopoulou et al. 2017). Combined force plate and kinematic (including X-ray cineradiographic) analyses to estimate bone loading can be conducted in absence of direct strain gauge data as well (Biewener 1983b).

A current limitation to both strain gauge and kinetic/kinematic data analyses is a lack of data collected in the field. Laboratory experiments only assess a subset of behaviors that may not include the greatest loads experienced by the skeleton in nature. Telemetry systems have been used in the past, but have required large battery packs and thus could only be

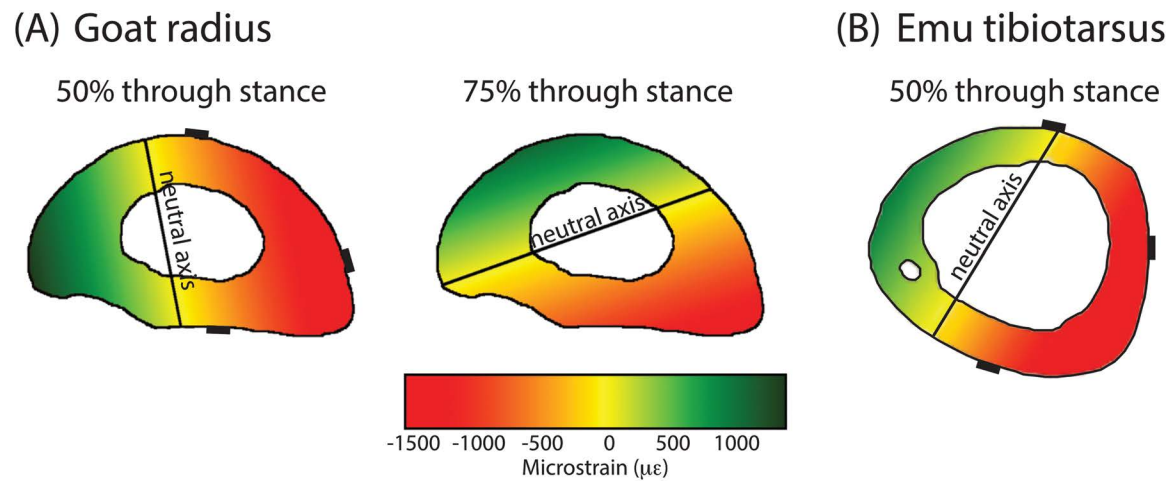

FIGURE 33.4 Normal (longitudinal) axial strain distributions for a goat radius and an emu tibiotarsus. A, The normal strain distribution in the goat radius shifts during the stance phase from mediolateral bending at 50% stance to nearly craniocaudal bending at 75% through stance, which is a shift of nearly 90° (Main and Biewener 2004). B, In contrast, the strain distribution in the emu tibiotarsus shows nearly mediolateral bending at midstance. Given the large amount of torsion present in this bone (Table 33.2), I_{MAX} and I_{MIN} are fairly similar, indicating a roughly circular bone (Main and Biewener 2007). Black rectangles on the bone surfaces indicate the position of the three strain gauges required to determine the normal strain distributions (Biewener 1992). The normal strain distributions are fairly independent of specific gauge positions (Verner et al. 2016), thus, it may be more useful to present the maximal predicted strains based on these normal strain models, rather than those measured from gauges located near the neutral axis.

carried by relatively large animals (Swartz et al. 1989, 1992). To assess bone strains in nature, miniaturized bridge amplifiers and data logging systems must be developed for the field of comparative biomechanics. This is the next critical step for advancing our understanding of the range of mechanical influences experienced by the skeleton in nature. Using such knowledge, we could begin to apply adaptive models, combining information about the range of strains experienced by the skeleton throughout a time period (days or weeks) and their frequency of occurrence over a given period of time (Fyhrie and Carter 1986, Beaupré et al. 1990, van der Meulen et al. 1993, Konieczynski et al. 1998, Fritton et al. 2000, Huiskes et al. 2000).

A number of methods can assess bone tissue mechanical properties at various levels of tissue organization. Whole bone strength (peak load, stress or strain) can be determined using a material testing system to load bones to yield or failure in uniaxial tension or compression, bending or torsion about a given axis. Because these loading modes are relatively simple, the peak stresses or strains engendered can be calculated using standard equations (Figure 33.2). Based on these biomechanical tests and measured or calculated *in vivo* bone loading, skeletal safety factors can be determined as:

$$\text{Safety factor} = \frac{\text{Peak } ex\ vivo \text{ stress (or strain)}}{\text{Peak } in\ vivo \text{ stress (or strain)}}$$

Safety factor provides some idea of how "overbuilt" a skeletal structure may be relative to the i*n vivo* forces experienced by the bone (Alexander 1981). The greater the safety factor, the less likely the bone is to fracture during a given mechanical activity. Cortical bone fails under compressive loading at ~20,000 με, but it begins to yield at 9800 με in compression and 8700 με in shear (Mirzaali et al. 2016, Morgan et al. 2018). Table 33.2 would indicate a wide range of potential safety factors, though many of them fall between 1.5 and 10 (Biewener 1993, Blob et al. 2014). All of the "standard" failure and yield strain values are from human or bovine bone (Table 33.1), establishing a clear need for axial and shear yield and failure properties from a broader comparative sample.

Whole bone strength depends on tissue-level material and structural properties. Tissue-level material properties can be determined for whole bone tests if the bone's structure or geometry can be properly measured or characterized. However, because whole bone structure is complex, involving nonuniform shapes and bone curvatures, strains calculated from *ex vivo* whole bone tests are approximate at best, which is why these tests are often conducted while directly collecting *ex vivo* strain gauge data (e.g., Blob and Biewener 1999, Blob et al. 2014).

Machining biological tissue samples of uniform and well-defined shape and size (e.g., prismatic rods or cubes) is the best way to experimentally measure bone tissue material properties at the meso- or microscale (e.g., Reilly and Burstein 1975, Lanyon et al. 1979). In these cases, the same load can be applied across a uniform structure where stress, strain, and elastic modulus can be accurately assessed. This approach represents an average of material characteristics over a heterogeneous material comprised of collagen, mineral, the OLCS, vasculature, and other porous spaces. However, this approach faithfully represents bone tissue as a functional unit that resists daily loading (Table 33.1). This type of approach has even been used to test individual secondary osteons by isolating them from the surrounding bone tissue to understand relationships between collagen fiber orientation and osteon strength and stiffness (Ascenzi and Bonucci 1967, 1968, Ascenzi et al. 1990, 1994).

At a micro- and nanostructural level, bone tissue can vary in its mechanical properties in relation to bone material density (mineral crystals per volume of bone), protein composition and content, and the chemical interactions among collagen and other proteins. While changes in the mineral and proteins at this scale can affect whole bone material properties, such changes can be probed specifically using ultrasonography and micro- and nanoindentation instruments. Many biomedical rodent models have shown how aging, genetics, dietary alterations, and disease can cause changes in mineral and collagen composition that affect nano- and tissue-level material properties (Mehta et al. 1999, Vashishth et al. 2001, Reumann et al. 2011, Donnelly et al. 2012, Gharpure et al. 2016, Hunt et al. 2019).

Bone material properties can vary among taxa and in relation to functional demands (Biewener 1982, Currey 1987, 1988, 2002, Currey and Pond 1989, Brear and Currey 1990, Casinos and Cubo 2001, Erickson et al. 2002). Classic studies by John Currey showed the dependence of BMD and the associated differences in bone material properties to *in vivo* function for the whale tympanic bulla, the cow femur and the cervid antler (Currey 1979). This example demonstrates how BMD strongly influences bone material properties in relation to function. The highly mineralized whale bulla is very stiff and does not absorb much mechanical energy prior to fracture (i.e., brittle). The cervid antler is at the other end of the spectrum, having relatively low mineralization, but capable of absorbing a relatively high amount of mechanical energy prior to fracture (i.e., tough). For the whale bulla, the forces it has evolved to withstand are low magnitude vibrational energies, but they must be transmitted with little loss of energy for effective sensation, so toughness is sacrificed for stiffness (Figure 33.1C). In the antler, faithful transmission of force is less important than simply not breaking, so toughness through relatively low matrix mineralization is selected. The cow femur is intermediate between the two in mineralization, representing a selective compromise between toughness and stiffness. Thus, collagen composition, bone chemistry and BMD are important compositional features that can be favored evolutionarily. However, outside Currey's work, the breadth of vertebrate bone properties in relation to mechanical function is not well understood.

Modeling Musculoskeletal Biomechanics

The classic approach for modeling a structure under load is by conducting free body diagram (FBD) analysis on a static loading condition. The same can be done for dynamic musculoskeletal movements by analyzing a sequence of instantaneous "static" moments in time. To do this, the structure of the bone (or tooth, or other solid structure) being analyzed must be measured for the relevant lengths and dimensions (cross-sectional areas, lengths, radius of curvature, second moments of area), and the various forces acting on it must be evaluated. Development of an exhaustive accounting of the forces acting on the bone often requires a number of measures and assumptions.

First, the joint kinematics or position of the bone in three-dimensional (3D) space relative to external forces needs to be known to assess the orientations of the external forces relative to the bone (Figure 33.5). This can be done *in vivo* using high-speed video or cineradiography. This approach, even when used in natural settings, still requires idealized conditions and some control over the experimental setup (McGowan et al. 2005, Hedrick and Biewener 2007). When *in vivo* motion

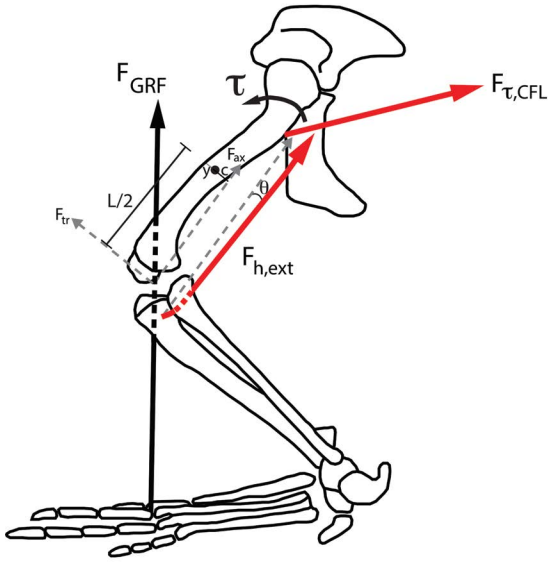

FIGURE 33.5 A simplified example of forces and moments to consider in a free body diagram (FBD) of the *Alligator* hindlimb. Limb kinematics were determined using X-ray cineradiographic video. The ground reaction force (F_{GRF}) was taken from published midstance values for *Alligator* (Blob and Biewener 1999, 2001). This example only considers flexion/extension moments on the femur caused by components of the F_{GRF} (F_{tr}, F_{ax}) and the hip extensor moment ($F_{h,ext}$). The torsional stress caused by the force of the *m. caudofemoralis longus* acting on the proximal femur is also shown. Not shown are the antagonistic knee extensors that counter the knee flexion caused by $F_{h,ext}$ or the torsional moment caused by F_{GRF} on the femur. All axial forces must act parallel to the femur. Therefore, a local coordinate system based on femoral position is established and muscle and GRF moments are resolved relative to that. In axial compression, the GRF component parallel to the long axis of the femur (F_{ax}) and the axial component of $F_{h,ext}$ are considered, where θ equals the angle between $F_{h,ext}$ and its component parallel to the femur's long axis. Bending stresses consider the transverse bending force of the GRF (F_{tr}) and the length at which this force is applied from the midshaft (*L*/2). Subtracted from this value are the bending moments induced by F_{ax} acting about the bone's curvature (*c*) and the component of $F_{h,ext}$ acting transverse to the bone's long axis [$F_{h,ext}(\sin\theta)$] (not shown). The midshaft torsional moment is calculated as the torsional force applied to the proximal femur ($F_{\tau,CFL}$) times the distance from the midshaft centroid to the midshaft bone surface (*y*), over the polar moment of inertia (*J*). (Complete details for this type of FBD reconstruction can be found in Biewener 1983b and Blob and Biewener 2001.)

capture is not possible to collect, some estimation of the possible positions of the bones relative to external forces must be assumed. The possible position of the limbs can be constrained based on skeletal and soft tissue anatomy to determine realistic ranges of motion for the element of interest (Kambic et al. 2017, Manafzadeh and Padian 2018).

Following a measure or estimate of possible skeletal positions during the load cycle, the reaction forces on the skeletal element must be determined, whether this be the force exerted by a piece of food on the teeth/jaw, the force of the ground pushing back on the limb of a running animal, the aerodynamic forces acting on a wing during flight or the hydrodynamic forces acting on an appendage during swimming. This is best done directly using force plates for terrestrial locomotion, bite force sensors for feeding or wing-mounted pressure sensors and accelerometers or digital particle image velocimetry (DPIV) for flying or swimming animals. However, these approaches are not always accessible. In such cases, we must rely on biomechanical theory using, for example, the known or estimated body weight (BW) of the animal and the calculated forces required to keep the center of mass of that animal from falling to the earth, based on the kinematic position of the limb. This is more easily done if a definitive two-dimensional (2D) or 3D position of the limb is known. If not, the number of assumptions becomes compounded by having to estimate limb position, in addition to BW, and the various external mechanical forces that may act on the limb. In some cases, one could argue that the amount of speculation may outweigh the utility of the approach; though some examples presented later provide creative solutions to such cases.

Beyond the reaction forces applied to the skeletal element of interest, there are also muscles that exert force on or across a limb element. These muscles can apply tension directly to the area of interest on the bone itself, or apply force across the length and curvature of the bone, which can impose bending loads on the bone (Figure 33.5). It is possible to measure muscle forces directly in some unique anatomical conditions. For example, if a muscle or group of muscles inserts on the bone through a common tendon, strain gauge-based tendon buckle readings from that tendon can be calibrated to determine the muscle forces conveyed to the skeleton through that tendon (Biewener et al. 1988, Biewener 1992, Richards and Biewener 2007). These anatomical conditions are rare, however, and the vast majority of FBD analyses rely on indirect estimates of muscle force. Using the ground reaction forces exerted on the musculoskeletal system and anatomical limb position, the muscle forces required to maintain limb position are calculated about a joint (Figure 33.5). Often, several muscles spanning a joint may have a similar function; the composite force acting through these muscles can be calculated singly or as a group based on relative muscle mass. The stress attributed to vertebrate muscle during maximal power output is 300 kN m^{-2} (kPa; Close 1972) and is normalized to maximal muscle force based on the physiological cross-sectional area (PCSA) of the muscle. Typically, when both flexor and extensor muscles cross a joint, the muscles unlikely to contribute to the modeled function are ignored (for example, uniarticular hip flexors during the stance phase of running). However, many muscles are multiarticular and contribute forces across more than one joint. These muscles, even if not of interest to moment calculations about the joint of interest (e.g., extensor moment about the hip), must still be accounted for to calculate the forces present in the antagonistic muscles acting about the joint of interest (e.g., knee flexor action of a hip extensor being countered by a knee extensor during running to maintain a static knee). These estimates will increase the complexity of the musculoskeletal model. The presence of antagonistic muscle forces in these models would produce an infinite number of possible answers when trying to balance joint moments in an FBD analysis. This situation is typically avoided by minimizing the amount of force required by the muscles to balance the ground reaction force moment against the moments created by antagonistic muscles (Blob and Biewener 2001). However, it should be recognized that this approach may generate a minimum estimation of muscle-induced bone stress (or strain) within the limb.

Once the external and muscle forces have been validated, they can be applied about the bone with a known length, curvature, cross-sectional shape, and material properties to resolve the transverse (bending), longitudinal (axial) and torsional force components acting on a bone, which can then be used to calculate the axial, bending and shear stresses and strains that the bone experiences (Figure 33.5). It is obvious that the more assumptions that are made in the process, the more tenuous the calculated bone stresses and strains become.

FBD solutions are perfectly acceptable in many situations as long as proper boundary conditions can be applied and balanced. There are situations where the skeletal morphology or motions of interest are very complex and *in vivo* measures cannot be made to use for validation. In these cases, the best option is to use computational approaches. Finite element analyses (FEA) use 2D or 3D computational models to calculate estimates of the stresses and strains produced in a structure of interest. These computational techniques have been employed for decades in mechanical and biomedical engineering fields, but they have also been used in comparative mechanical studies for at least the last 30 years (Beaupré et al. 1990, Carter et al. 1991, Rensberger 1995). These analyses require the same 3D structural, material property, and external force inputs required by FBD analyses. However, by using this computational approach it is possible to extend the single-site analysis common in the FBD approach to the entire bone or structural unit of choice. Using these approaches, it would be possible to estimate stress or strain across an entire bone. Such knowledge can inform possible hypotheses about mechanical adaptations regarding the evolution of skeletal morphology relative to regions of low safety factor, which may indicate anatomical regions under increased selection relative to others. As with an FBD analysis, there are many assumptions that may go into FEA models, so a greater level of confidence can be placed in their conclusions if they are validated with direct mechanical measures of *in vivo* or *ex vivo* strain data (Porro et al. 2013, Yang et al. 2014, Panagiotopoulou et al. 2017). This additional validation provides greater confidence in the assumptions about other mechanical and material variables in the model, otherwise the entire model comes with the caveat that the resulting mechanical data may not be valid.

In the last 10 to 15 years, advances in technical hardware, software and computational processing speed have allowed more advanced computational methods in developing musculoskeletal models. Detailed anatomical models of the skeletal system performing different mechanical functions can be developed using 3D X-ray cineradiography units (X-ray reconstruction of moving morphology [XROMM]) (Brainerd et al. 2010). These detailed kinematic models can be incorporated into complex musculoskeletal models for estimating muscle forces while reproducing realistic skeletal motions. Comparative reconstructions of muscular function have been increasingly examined using software for interactive musculoskeletal modeling (SIMM), OpenSim, or multidynamics analyses (MDA) (Delp and Loan 1995, Delp et al. 2007, Curtis et al. 2008). Integration of these models with data from experimental biomechanical sensors (EMG recordings, strain gauge and tendon buckle measures) increases the robusticity of these methods. Because invasive *in vivo* techniques are not available for many living taxa of interest or in paleontological studies, these computational approaches are being increasingly used in comparative biomechanical and paleontological studies as well (Hutchinson et al. 2005, 2015, Curtis et al. 2010, Rankin et al. 2018). Incorporating advanced imaging techniques such as CT and micro-CT, that can help to distinguish soft tissues such as cartilage, muscles, ligaments and tendons, could allow the development of complete, 3D musculoskeletal models from preserved museum specimens (Charles et al. 2016, Tsai et al. 2020). These combined anatomical and mechanical modeling approaches provide methodologies to test a broad array of functional musculoskeletal and evolutionary hypotheses, with a higher degree of confidence and sensitivity than ever before.

Ultimately, an integrated approach to *in vivo* musculoskeletal biomechanics would include an assessment of 3D motion of the skeletal limb elements with EMG measures of key muscles being used to inform SIMM or MDA musculoskeletal models overlying the skeletal reconstructions. Information gleaned from these models could be used as external force inputs for FEA models of the bone(s) of interest with the computational strains being validated by attaching strain gauges to the bones during skeletal movement. This would provide a truly integrated view of muscle and bone function during a variety of activities. However, there are few research labs capable of conducting this integrated approach, which speaks to the ever-increasing need for cross-disciplinary research among engineers, comparative biomechanists and paleontologists.

Application of Biomechanical Analyses to Paleontological and Comparative Questions of Function

Although no studies have accomplished all of the above *in vivo* and computational techniques in a single biomechanical study, many studies have used several *in vivo* mechanics and modeling sensitivity analyses to validate biting or locomotor musculoskeletal mechanics in living and extinct animals. Below are two examples, mastication in primates and theropod locomotor mechanics. These examples highlight some of the considerations necessary for collecting *in vivo* biomechanical data and appropriating that data, using the proper sensitivity analyses, to test functional hypotheses about living and fossil species.

Biting Mechanics in Primates

In reconstructing musculoskeletal biting mechanics in extant and fossil primates, it is necessary to account for musculoskeletal anatomy, EMG activity of the active masticatory muscles, material properties of the facial skeleton, and (if possible) *in vivo* bone strains collected from a number of different sites on the skull. Many of the *in vivo* EMG and bone strain data in the primate skull (macaques, humans) have been known for some time (e.g., Hylander 1977, Hylander et al. 1987, 1992, 1998, 2000, Hylander and Johnson 1997, Ross 2001, Ross et al. 2005, Smith et al. 2015a).

As computational FE modeling for quasi-static loading and biologists' interest in applying them to comparative biological systems grew, elastic properties were determined for the mandible and cranium of some primate species (Peterson and Dechow 2003, Wang and Dechow 2006, Davis et al. 2011, Gharpure et al. 2016). In addition to these data on bone properties, information on the muscle forces acting on the skull is also required. Estimation of peak force is relatively straightforward, and it has been approached with basic muscle anatomy and EMG activation data (Ross et al. 2005, Stansfield et al. 2018a). However, a more elegant approach is through using MDA, where both cranium and mandible can be modeled, muscles separated in distinct subsegments, wrapped around the cranium where needed, and made to act (computationally) as a functioning system to derive muscle forces and moments for input into FE models (Figure 33.6A) (Grosse et al. 2007, Curtis et al. 2008, Fitton et al. 2012, Liu et al. 2012, Shi et al. 2012). FE modeling of primate skulls was conducted with realistic input forces, material properties and bone strain validation data. To be sure, FE modeling is possible even if only the anatomy is known, but to be realistic and valid, these other mechanical factors should be incorporated as well. The groups conducting these studies have, in general, been very careful regarding sensitivity analyses and applying them to understand the effects of (for example) the distribution of material properties in the skull, the presence/absence and activity of different muscle groups, and the presence of cranial sutures on the resulting cranial stress and strain patterns (Ross et al. 2005, Strait et al. 2005, Kupczik et al. 2007, Fitton et al. 2012, Gröning et al. 2012, 2013, Stansfield et al. 2018a). More recently, the combination of sensitivity analyses and geometric morphometrics has arisen as a way of understanding how deformation in response to different loading conditions or variation within a population of animals might be important for interpreting analyses of extant and extinct species (Fitton et al. 2012, Smith et al. 2015a). By the time these same approaches were applied to *Australopithecus africanus* (*A. africanus*), *A. sediba*, *Paranthropus boisei* and ancient populations of *Homo*, there was already a wealth of data regarding sensitivity analyses and their effects on model outcomes in efforts to tests hypotheses about evolutionary changes relative to corresponding changes in cranial and mandibular morphology (Figure 33.6B) (Strait et al. 2009, Smith et al. 2015b, Ledogar et al. 2016, Stansfield et al. 2018b).

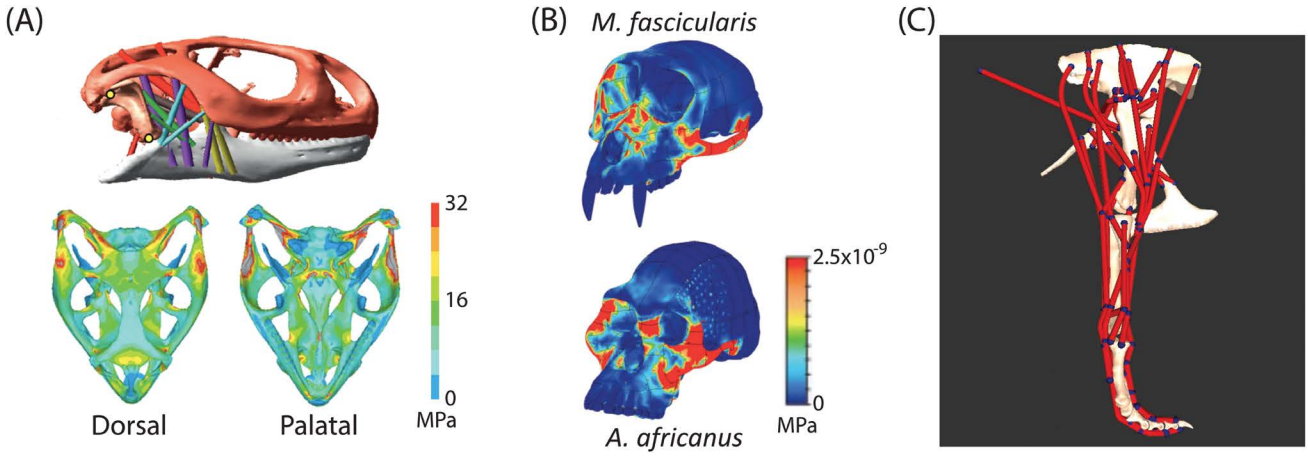

FIGURE 33.6 Computational biomechanical modeling applied to extant and extinct taxa. A, Multibody dynamics and finite element analysis (FEA) of *Uromastyx hardwickii*. The multidynamics analysis (MDA) models bilateral muscle activity of seven distinct pairs of muscle bellies on jaw adduction. Constraints on the system are two quadrate-based joints (yellow circles), a temporal ligament (in light blue), three fixed points on the occipital condyle, and material properties of the food particle. Food was bitten at the front of the mouth. Based on results from the MDA, boundary conditions (muscle forces, ligament forces, bite force and joint force) and bone and soft tissue properties were inputs for an FEA to determine the von Mises stress developed in the cranium during biting. The von Mises stress combines all the principal and shear stresses into a single number that is typically predictive of failure. B, FEA results for *Mulatta fascicularis* and *Australopithecus africanus* while biting with the postcanine teeth. Material properties for the cancellous and cortical bone and teeth were assigned. Four pairs of bilateral biting muscles were modeled. All of the postcanine teeth and articular eminences were constrained. Strain energy density is plotted here, which is similar to von Mises stress, and indicates a primarily distortional environment (as opposed to strains increasing the sample volume). C, A Software for Interactive Musculoskeletal Modeling (SIMM) model of a *Tyrannosaurus rex* hindlimb, showing the 37 unique muscle bellies modeled. Each muscle had a single origin and insertion point. Numerous muscles were subject to sensitivity analyses in regard to their muscle origins and wrapping surfaces around particular joints. Unrealistic net joint moments contrary to static standing were ruled out. The SIMM analysis used here suggests that *T. rex* had a mostly upright, but not columnar stance (hip flexion at 15°). (Figures were adapted from A, Moazen et al. 2008a, b; B, Strait et al. 2009; C Hutchinson et al. 2005.)

Other biting systems have been modeled in the bat, living and extinct crocodylomorphs and two lizards (*Uromastyx* and *Sphenodon*) (e.g., Dumont et al. 2005, Moazen et al. 2008a, b, Pierce et al. 2008, Curtis et al. 2010, 2011, Santana et al. 2012, Porro et al. 2013, 2014, Ballell et al. 2019). These papers all provide examples of the issues discussed above applied across a broad range of comparative species. A number of general reviews for the use of finite element models and geometric morphometrics, including their limitations and sensitivity considerations, have been published and are recommended for further review (Rayfield 2007, Dumont et al. 2009, O'Higgins et al. 2012, 2019, Panagiotopoulou et al. 2012, Polly et al. 2016).

Modeling Locomotion in Theropods

The examples provided above involve motion in the jaw and cranium during mastication. While efficiency and reduction of injury in eating are certainly important selective factors, the motion in itself can be reduced to a relatively simple rotational action controlled by relatively few constraints acting in the jaw. This is not nearly as complex as movement about the proximal joints of the limbs during locomotion where flexion/extension, abduction/adduction and long axis rotation are all valid for consideration in modeling limb motion in living and extinct taxa. Historically, limb motions were modeled only in flexion and extension and were largely confined to the study of mammals and terrestrial birds between 1970 and 1990. However, in the last 20 years, kinematic, bone strain and EMG data in nonmodel taxa have allowed consideration of a larger range of motion for tetrapod limbs.

Reconstructing the locomotion of theropods, and archosaurs in general, has been attractive as a means of studying locomotion in nonavian dinosaurs. The anatomy, kinematics and muscle activation data from crocodilian and bird species, as well as their importance in the evolution of birds, have been described (Gatesy 1991, 1997, 1999a, b, Gatesy and Biewener 1991, Gatesy and Dial 1996, Reilly and Elias 1998, Hutchinson 2001, 2002). Early musculoskeletal models were relatively simple, modeling the limb in flexion/extension and then abduction/adduction (Hutchinson and Garcia 2002, Hutchinson et al. 2005). Around this same time, *in vivo* femoral bone strains from extant archosaurs and lizards, including iguanas, alligators, chickens and emu, indicated that shear strains due to nonparasagittal long axis rotation is another important locomotor plane of motion to consider (Carrano and Biewener 1999, Blob and Biewener 1999, 2001, Main and Biewener 2007), even when avian archosaurs appear to be moving in a fairly parasagittal way (Hutchinson and Gatesy 2000, Kambic et al. 2017). A *Tyrannosaurus rex* musculoskeletal model in SIMM was used to run sensitivity analyses on muscle paths, origin and insertion centroids (where ambiguous), and muscle wrapping at the joints (Hutchinson et al. 2005) (Figure 33.6C). This locomotor simulation of *T. rex* used 3D scans of a museum sample to reconstruct a computational anatomical model, used assumptions about the scaling of muscle masses, and used basic tetrapod muscle physiological properties to determine optimum muscle moments generated by each of the 37 limb

muscles when holding the limb at different positions. The results suggested that the greatest mechanical advantage for the muscles occurs over a limited period of limb excursion, which would make it unlikely that *T. rex* could generate the necessary muscle forces required to run with a typical bipedal aerial phase. This conclusion was confirmed using a different theropod limb flexion/extension, constraints-based exclusion approach to determine, using a number of anatomical, kinematic and kinetic constraints, that large theropods could only generate 1.0–1.5 BW of force in each limb, and not the ~2.0 BW required for bipedal running (Gatesy et al. 2009).

A recent 3D analysis of ostrich hindlimb biomechanics found that ostrich muscles do not actually operate at peak muscle force and moment efficiency during slow running, which prior theropod models had assumed (Hutchinson et al. 2015). This study also showed the importance of examining the hindlimb joints of animals in 3D planes and laid an important foundation to understand how the balance of muscle and external forces act in the hindlimb joints of birds. An impressive series of recent studies have combined SIMM models and FEA to predict the evolution of cancellous bone structure in the hindlimbs of avian and nonavian theropods. Boundary conditions for the FE models were based on both muscle forces and soft tissue constraints at the joints. Sensitivity analyses for variation in bone and soft tissue structures were not accounted for. However, given the complex analyses and scope of this work, simplifying assumptions such as these had to be made and are identified in the studies (Bishop et al., 2019a, b, c). Whereas these works represent a complex assessment of limb kinematics, ground reaction forces, anatomical anatomy and computational modeling, this is certainly not the entire hindlimb constraint space that could have been used. Noticeably missing from this model is some assessment of skeletal biomechanics. Mapping these limb motions and muscle reconstructions to an *in vivo* measure of skeletal mechanics provides one more validation constraint on the larger computational model.

Recent use of XROMM has addressed some of the problems of soft tissue constraints in archosaurs, where crocodilians and different avian taxa have been used to distinguish between *in vivo* range of motion, *ex vivo* soft tissue range of motion and *ex vivo* skeletal range of motion (Kambic et al. 2017, Manafzadeh and Padian 2018, Tsai et al. 2020). The most revealing of these examined guinea fowl moving through an XROMM imaging volume performing different functions compared to motions in the same joints in cadaveric birds (Kambic et al. 2017). This study showed that a very small portion (~30%) of the *ex vivo* 3D movement space is actually used *in vivo*. It also indicated that the limitation of constraining limb motion in paleontological and comparative studies is the lack of knowledge regarding the role of specific soft tissue constraints in limiting joint movement. More recently, crocodiles and quail have been examined to study the role of soft tissues, including ligaments, soft tissue bursae and cartilage caps in comparative skeletal range of motion analyses (Manafzadeh and Padian 2018, Tsai et al. 2020).

Nyakatura et al. (2019) recently reconstructed the gait of the Permian stem amniote *Orobates pabsti*. This novel study used kinematics and kinetics from a range of extant comparable taxa, 3D skeletonization of *Orobates* and an informed sensitivity and constraints-based gait exclusion approach to reconstruct the gait of *Orobates*, based on a known fossil trackway. This combination of approaches could serve as a model for further efforts to reconstruct locomotion in extinct taxa.

Conclusion

Bone is both a living organ and rigid support element. To the strength of the rigid support is added adaptive and reparative mechanisms that can sustain bone's strength and toughness through an animal's lifetime to the variety of functions the bone must serve. Bone is composed of both collagen and hydroxyapatite mineral that provides it strength in tensile, compressive and torsional loading. In addition, the density and distribution of these materials can provide different regions of the skeleton different mechanical attributes. Functional adaptation of the skeleton can modify these attributes and differentially alter a bone's safety factor during an animal's lifetime, preventing fatigue or catastrophic damage. The stresses and strains that the skeleton must withstand during life can be measured using a number of different techniques, each with its own strengths and limitations, to measure anatomical structures, motion of the skeleton, forces exerted by the skeleton, how those forces are transmitted to deformation of the skeleton, and the muscle activations responsible for skeletal and ground reaction force loading. These approaches can be combined with advanced measures of 3D skeletal movement (XROMM), FEA, MDA, and musculoskeletal SIMM modeling as a form of validation for these computational models that are often used to address more complex functional hypotheses in extant and extinct taxa.

Although we have an extraordinary array of measurement tools that allow us to learn more about musculoskeletal cell biology and mechanics, there are limitations in all of these approaches and we must be careful to validate our models and perform the necessary sensitivity analyses when applying these computational methods to new taxa. We must also realize that there is a vast amount of variation in biomechanical measurements because of differences in basic morphology, and not *all* questions require *all* kinematic, kinetic or material parameters to be known. For example, if similar taxa are being compared, perhaps similar material properties of biological tissues can be assumed. If the question asked is of a broad enough scope, perhaps some small detail about kinematics can be ignored. Regardless, in all cases, this must be rationalized and transparent to the reader. Otherwise, our ability to reproduce experimental results or use similar approaches to test related hypotheses is limited.

Acknowledgments

I give my deep thanks to Dr. Richard Blob for his critical comments on this manuscript and for providing references for Table 33.2. Dr. Callum Ross assisted with gathering references and clarifying data for Table 33.2. Dr. Corwin Sullivan provided the cineradiographic video to reproduce the *Alligator* kinematics for Figure 33.5. This work was supported in part by the National Science Foundation CMMI 1463523.

REFERENCES

Aamodt, A., et al. 1997. *In vivo* measurements show tensile axial strain in the proximal lateral aspect of the human femur. *J. Orthop. Res.* 15: 927–931.

Aiello, B. R., et al. 2013. Correlation of muscle function and bone strain in the hindlimb of the river cooter turtle (*Pseudemys concinna*). *J. Morphol.* 274: 1060–1069.

Alexander, R. M. N. 1981. Factors of safety in the structure of animals. *Sci. Progr.* 67: 109–130.

Ascenzi, A. and E. Bonucci. 1967. The tensile properties of single osteons. *Anat. Rec.* 158: 375–386.

Ascenzi, A. and E. Bonucci. 1968. The compressive properties of single osteons. *Anat. Rec.*161: 377–391.

Ascenzi, A., et al. 1990. The bending properties of single osteons. *J. Biomech.* 23: 763–771.

Ascenzi, A., et al. 1994. The torsional properties of single selected osteons. *J. Biomech.* 27(7): 875–884.

Ballell, A., et al. 2019. Convergence and functional evolution of longirostry in crocodylomorphs. *Palaeontology* 62: 867–887.

Bartel, D. L., et al. 2006. *Orthopaedic biomechanics.* Upper Saddle River, NJ, Pearson Education.

Beaupré, G. S., et al. 1990. An approach for time-dependent bone modeling and remodeling - application: A preliminary remodeling simulation. *J. Orthop. Res.* 8: 651–661.

Bertram, J. E. A. and A. A. Biewener. 1988. Bone curvature: Sacrificing strength for load predictability? *J. Theor. Biol.* 131: 75–92.

Biewener, A. A. 1982. Bone strength in small mammals and bipedal birds: Do safety factors change with body size? *J. Exp. Biol.* 98: 289–301.

Biewener, A. A. 1983a. Allometry of quadrupedal locomotion: The scaling of duty factor, bone curvature and limb orientation to body size. *J. Exp. Biol.* 105: 147–171.

Biewener, A. A. 1983b. Locomotory stresses in the limb bones of two small mammals: The ground squirrel and chipmunk. *J. Exp. Biol.* 103: 131–154.

Biewener, A. A. 1992. *In vivo* measurement of bone strain and tendon force. In *Biomechanics: structures and systems. A practical approach*, 123–148. New York, Oxford University Press.

Biewener, A. A. 1993. Safety factors in bone strength. *Calcif. Tissue Int.* 53(Suppl 1): S68–S74.

Biewener, A. A. and K. P. Dial. 1995. *In vivo* strain in the humerus of pigeons (*Columba livia*) during flight. *J. Morphol.* 225: 61–75.

Biewener, A. A. and C. R. Taylor. 1986. Bone strain: A determinant of gait and speed? *J. Exp. Biol.* 123: 383–400.

Biewener, A. A., et al. 1988. Muscle forces during locomotion in kangaroo rats: Force platform and tendon buckle measurements compared. *J. Exp. Biol.* 137: 191–205.

Biewener, A. A., et al. 1996. Adaptive changes in trabecular architecture in relation to functional strain patterns and disuse. *Bone* 19: 1–8.

Biewener, A. A., et al. 1986. Bone modeling during growth: Dynamic strain equilibrium in the chick tibiotarsus. *Calcif. Tissue Int.* 39: 390–395.

Bishop, P. J., et al. 2019a. Cancellous bone and theropod dinosaur locomotion. Part I—an examination of cancellous bone architecture in the hindlimb bones of theropods. *PeerJ.* 6: e5778.

Bishop, P. J., et al. 2019b. Cancellous bone and theropod dinosaur locomotion. Part II—a new approach to inferring posture and locomotor biomechanics in extinct tetrapod vertebrates. *PeerJ.* 6: e5779.

Bishop, P. J., et al. 2019c. Cancellous bone and theropod dinosaur locomotion. Part III—Inferring posture and locomotor biomechanics in extinct theropods, and its evolution on the line to birds. *PeerJ*, 6: e5777.

Blob, R. W. and A. A. Biewener. 1999. *In vivo* locomotor strain in the hindlimb bones of *Alligator mississippiensis* and *Iguana*: Implications for the evolution of limb bone safety factor and non-sprawling limb posture. *J. Exp Biol.* 202: 1023–1046.

Blob, R. W. and A. A. Biewener. 2001. Mechanics of limb bone loading during terrestrial locomotion in the green iguana (*Iguana iguana*) and American alligator (*Alligator mississippiensis*). *J. Exp. Biol.* 204: 1099–1122.

Blob, R. W., et al. 2014. Diversity of limb-bone safety factors for locomotion in terrestrial vertebrates: Evolution and mixed chains. *Integr. Comp. Biol.* 54: 1058–1071.

Bouxsein, M., et al. 2010. Guidelines for assessment of bone microstructure in rodents using micro-X-ray reconstruction tomography. *J. Bone Miner. Res.* 25: 1468–1486.

Brainerd, E. L., et al. 2010. X-Ray reconstruction of moving morphology (XROMM): Precision, accuracy and applications in comparative biomechanics research. *J. Exp. Zool. A* 313: 262–279.

Brear, K. and J. D. Currey. 1990. Ontogenetic changes in the mechanical properties of the femur of the polar bear *Ursus maritimus*. *J. Zool. (Lond.) 222*: 49–58.

Buenzli, P. R. and N. A. Sims. 2015. Quantifying the osteocyte network in the human skeleton. *Bone* 75: 144–150.

Burr, D. B. and O. Akkus. 2014. Bone morphology and organization. In *Basic and applied bone biology*, eds. Burr, D. B. and M. R. Allen, 3–25. Amsterdam, Academic Press.

Burr, D. B., et al. 1985. Bone remodeling in response to *in vivo* fatigue microdamage. *J. Biomech.* 18: 189–200.

Butcher, M. T., et al. 2008. *In vivo* strains in the femur of river cooter turtles (*Pseudemys concinna*) during terrestrial locomotion: Tests of force-platform models of loading mechanics. *J. Exp. Biol.* 211: 2397–2407.

Butcher, M. T., et al. 2011. *In vivo* strains in the femur of the Virginia opossum (*Didelphis virginiana*) during terrestrial locomotion: Testing hypotheses of evolutionary shifts in mammalian bone loading and design. *J. Exp. Biol.* 214: 2631–2640.

Carrano, M. T. and A. A. Biewener. 1999. Experimental alteration of limb posture in the chicken (*Gallus gallus*) and its bearing on the use of birds as analogs for dinosaur locomotion. *J. Morphol.* 240: 237–249.

Carter, D. R. and G. S. Beaupré. 2001. *Skeletal function and form: Mechanobiology of skeletal development, aging, and regeneration*. Cambridge, UK, Cambridge University Press.

Carter, D. R. and W. C. Hayes. 1976. Bone compressive strength: The influence of density and strain rate. *Science* 194(4270): 1174–1211.

Carter, D. R., et al. 1976. Fatigue life of compact bone II. Effects of microstructure and density. *J. Biomech.* 9: 211–218.

Carter, D. R., et al. 1980. Measurement and analysis of *in vivo* bone strains on the canine radius and ulna. *J. Biomech.* 13: 27–38.

Carter, D. R., et al. 1991. Musculoskeletal ontogeny, phylogeny, and functional adaptation. *J. Biomech*. 24(Suppl. 1): 3–16.

Casinos, A. and J. Cubo. 2001. Avian long bones, flight and bipedalism. *Comp. Biochem. Physiol. A*131: 159–167.

Charles, J. P., et al. 2016. Muscle moment arms and sensitivity analysis of a mouse hindlimb musculoskeletal model. *J. Anat.* 229: 514–535.

Close, R. I. 1972. Dynamic mammalian properties of skeletal muscles. *Physiol. Rev.* 52: 129–197.

Copploe, J. V., et al. 2015. In vivo strains in the femur of the nine-banded armadillo (*Dasypus novemcinctus*). *J. Morphol*. 276: 889–899.

Cowin, S. C., et al. 1995. A case for bone canaliculi as the anatomical site of strain generated potentials. *J. Biomech*. 28: 1281–1297.

Currey, J. D. 1979. Mechanical properties of bone tissues with greatly differing functions. *J. Biomech*. 12: 313–319.

Currey, J. D. 1987. The evolution of the mechanical properties of amniote bone. *J. Biomech*. 20: 1035–1044.

Currey, J. D. 1988. The effect of porosity and mineral content on the Young's modulus of elasticity of compact bone. *J. Biomech*. 21: 131–139.

Currey, J. D. 1999. What determines the bending strength of compact bone? *J. Exp. Biol*. 202: 2495–2503.

Currey, J. D. 2002. *Bones: Structure and mechanics*. 1st ed. Princeton, NJ, Princeton University Press.

Currey, J. D. and C. M. Pond. 1989. Mechanical properties of very young bone in the axis deer (*Axis axis*) and humans. *J. Zool. (Lond.)* 218: 59–67.

Curtis, N., et al. 2008. Predicting skull loading: Applying multibody dynamics analysis to a macaque skull. *Anat. Rec.* 291: 491–501.

Curtis, N., et al. 2010. Comparison between *in vivo* and theoretical bite performance: Using multi-body modelling to predict muscle and bite forces in a reptile skull. *J. Biomech*. 43: 2804–2809.

Curtis, N., et al. 2011. Functional relationship between skull form and feeding mechanics in *Sphenodon*, and implications for diapsid skull development. *PLoS One* 6: 31–33. https://doi.org/10.1371/journal.pone.0029804

Davis, J. L., et al. 2011. An efficient method of modeling material properties using a thermal diffusion analogy: An example based on craniofacial bone. *PLoS One*, 6: e17004. https://doi.org/10.1371/journal.pone.0017004

Delp, S. L. and J. P. Loan. 1995. A graphics-based software system to develop and analyze models of musculoskeletal structures. *Computers in Biol. Med. 25*: 21–34.

Delp, S. L., et al. 2007. OpenSim: Open-source software to create and analyze dynamic simulations of movement. *IEEE Trans. Biomed. Eng.* 54: 1940–1950.

Demes, B., et al. 1998. Patterns of strain in the macaque ulna during functional activity. *Am. J. Phys. Anthropol*. 106: 87–100.

Demes, B., et al. 2001. Patterns of strain in the macaque tibia during functional activity. *Am. J. Phys. Anthropol*. 116: 257–265.

D'Emic, M. D. and R. B. J. Benson. 2013. Measurement, variation, and scaling of osteocyte lacunae: A case study in birds. *Bone* 57: 300–310.

Donnelly, E., et al. 2012. Reduced cortical bone compositional heterogeneity with bisphosphonate treatment in postmenopausal women with intertrochanteric and subtrochanteric fractures. *J. Bone Miner. Res*. 27: 672–678.

Dumont, E. R., et al. 2005. Finite-element analysis of biting behavior and bone stress in the facial skeletons of bats. *Anat. Rec. A*283: 319–330.

Dumont, E. R., et al. 2009. Requirements for comparing the performance of finite element models of biological structures. *J. Theor. Biol*. 256: 96–103.

Easley, S. K., et al. 2010. Contribution of the intra-specimen variations in tissue mineralization to PTH- and raloxifene-induced changes in stiffness of rat vertebrae. *Bone* 46: 1162–1169.

Erickson, G. M., et al. 2002. Evolution of the biomechanical material properties of the femur. *Anat. Rec*. 268: 115–124.

Fitton, L. C., et al. 2012. Masticatory loadings and cranial deformation in *Macaca fascicularis*: A finite element analysis sensitivity study. *J. Anat*. 221: 55–68.

Fritton, S. P. and C. T. Rubin. 2001. *In vivo* measurement of bone deformations using strain gauges. In *Bone mechanics handbook*, 2nd ed., ed. Cowin, S. C., 8–41. Boca Raton, FL, CRC Press.

Fritton, S. P. and S. Weinbaum. 2009. Fluid and solute transport in bone: Flow-induced mechanotransduction. *Ann. Rev. Fluid Mech.* 41: 347–374.

Fritton, S. P., et al. 2000. Quantifying the strain history of bone: Spatial uniformity and self-similarity of low-magnitude strains. *J. Biomech*. 33: 317–325.

Fyhrie, D. P. and D. R. Carter. 1986. A unifying principle relating stress to trabecular bone morphology. *J. Orthop. Res.* 4: 304–317.

Gatesy, S. M. 1991. Hind limb movements of the American alligator (*Alligator mississippiensis*) and postural grades. *J. Zool*. 224: 577–588.

Gatesy, S. M. 1997. An electromyographic analysis of hindlimb function in *Alligator* during terrestrial locomotion. *J. Morphol*. 234: 197–212.

Gatesy, S. M. 1999a. Guineafowl hind limb function. I: Cineradiographic analysis and speed effects. *J. Morphol*. 240: 115–125.

Gatesy, S. M. 1999b. Guineafowl hind limb function. II: Electromyographic analysis and motor pattern evolution. *J. Morphol*. 240: 127–142.

Gatesy, S. M. and A. A. Biewener. 1991. Bipedal locomotion: Effects of speed, size and limb posture in birds and humans. *J. Zool*. 224: 127–147.

Gatesy, S. M. and K. P. Dial. 1996. Locomotor modules and the evolution of avian flight. *Evolution* 50: 331.

Gatesy, S. M., et al. 2009. Constraint-based exclusion of limb poses for reconstructing theropod dinosaur locomotion. *J. Vert. Paleontol*. 29: 535–544.

Gharpure, P., et al. 2016. Elastic properties of chimpanzee craniofacial cortical bone. *Anat. Rec*. 299: 1718–1733.

Goodship, A. E., et al. 1979. Functional adaptation of bone to increased stress. *J. Bone Joint Surg.* 61A: 539–546.

Gröning, F., et al. 2012. Modeling the human mandible under masticatory loads: Which input variables are important? *Anat. Rec*. 295: 853–863.

Gröning, F., et al. 2013. The importance of accurate muscle modelling for biomechanical analyses: A case study with a lizard skull. *J. R. Soc. Interface* 10(84): 20130216. https://doi.org/10.1098/rsif.2013.0216

Gross, T. S., et al. 1992. Characterizing bone strain distribution *in vivo* using three triple rosette strain gages. *J. Biomech*. 25: 1081–1087.

Grosse, I. R., et al. 2007. Techniques for modeling muscle-induced forces in finite element models of skeletal structures. *Anat. Rec.* 290: 1069–1088.

Hedrick, T. L. and A. A. Biewener. 2007. Low speed maneuvering flight of the rose-breasted cockatoo (*Eolophus roseicapillus*). I. Kinematic and neuromuscular control of turning. *J. Exp. Biol.* 210: 1897–1911.

Herring, S. W. and S. Teng. 2000. Strain in the braincase and its sutures during function. *Am. J. Phys. Anthropol.* 112: 575–593.

Herring, S. W., et al. 2005. Ontogeny of bone strain: The zygomatic arch in pigs. *J. Exp. Biol.* 208: 4509–4521.

Huiskes, R., et al. 2000. Effects of mechanical forces on maintenance and adaptation of form in trabecular bone. *Nature*, 405(6787): 704–706.

Hunt, H. B., et al. 2019. Altered tissue composition, microarchitecture, and mechanical performance in cancellous bone from men with type 2 diabetes mellitus. *J Bone Miner. Res.* 34: 1191–1206. https://doi.org/10.1002/jbmr.3711

Hutchinson, J. R. 2001. The evolution of pelvic osteology and soft tissues on the line to extant birds (Neornithes). *Zool. J. Linn. Soc.* 131: 123–166.

Hutchinson, J. R. 2002. The evolution of hindlimb tendons and muscles on the line to crown-group birds. *Comp. Biochem. Physiol. A* 133: 1051–1086.

Hutchinson, J. R. and S. M. Gatesy. 2000. Adductors, abductors, and the evolution of archosaur locomotion. *Paleobiology* 26: 734–751.

Hutchinson, J. R. and M. Garcia. 2002. *Tyrannosaurus* was not a fast runner. *Nature* 415(6875): 1018–1021.

Hutchinson, J. R., et al. 2005. Analysis of hindlimb muscle moment arms in *Tyrannosaurus rex* using a three-dimensional musculoskeletal computer model: Implications for stance, gait, and speed. *Paleobiology* 31: 676–701.

Hutchinson, J. R., et al. 2015. Musculoskeletal modeling of an ostrich (*Struthio camelus*) pelvic limb: Influence of limb orientation on muscular capacity during locomotion. *PeerJ* 2015: 1–52.

Hylander, W. L. 1977. *In vivo* bone strain in the mandible of *Galago crassicaudatus*. *Am. J. Phys. Anthropol.* 46: 309–326.

Hylander, W. L. 1979. Mandibular function in *Galago crassicaudatus* and *Macaca fascicularis*: An *in vivo* approach to stress analysis of the mandible. *J. Morphol.*159: 253–296.

Hylander, W. L. and R. Bays. 1979. An *in vivo* strain-gauge analysis of the squamosal-dentary joint reaction force during mastication and incisal biting in *Macaca mulatta* and *Macaca fascicularis*. *Arch. Oral Biol.* 24: 689–697.

Hylander, W. L. and K. R. Johnson. 1997. *In vivo* bone strain patterns in the zygomatic arch of macaques and the significance of these patterns for functional interpretations of craniofacial form. *Am. J. Phys. Anthropol.* 102: 203–232.

Hylander, W. L., et al. 1987. Loading patterns and jaw movements during mastication in *Macaca fascicularis*: A bone-strain, electromyographic, and cineradiographic analysis. *Am. J. Phys. Anthropol.* 72: 287–314.

Hylander, W. L., et al. 1992. Muscle force recruitment and biomechanical modeling: An analysis of masseter muscle function during mastication in *Macaca fascicularis*. *Am. J. Phys. Anthropol.* 88: 365–387.

Hylander, W. L., et al. 1991a. Function of the supraorbital region of primates. *Arch. Oral Biol.* 36: 273–281.

Hylander, W. L., et al. 1991b. Masticatory-stress hypotheses and the supraorbital region of primates. *Am. J. Phys. Anthropol.* 86: 1–36.

Hylander, W. L., et al. 1998. Mandibular corpus strain in primates: Further evidence for a functional link between symphyseal fusion and jaw-adductor muscle force. *Am. J. Phys. Anthropol.* 107: 257–271.

Hylander, W. L., et al. 2000. Symphyseal fusion and jaw-adductor muscle force: An EMG study. *Am. J. Phys. Anthropol.* 112: 469–492.

Kambic, R. E., et al. 2017. 3-D range of motion envelopes reveal interacting degrees of freedom in avian hind limb joints. *J. Anat.* 231: 906–920.

Kawano, S. M., et al. 2016. Comparative limb bone loading in the humerus and femur of the tiger salamander: Testing the "mixed-chain" hypothesis for skeletal safety factors. *J. Exp. Biol.* 219: 341–353.

Keller, T. S. and D. M. Spengler. 1982. *In vivo* strain gage implantation in rats. *J. Biomech.* 15: 911–917.

Keller, T. S. and D. M. Spengler. 1989. Regulation of bone stress and strain in the immature and mature rat femur. *J. Biomech.* 22: 1115–1127.

Kennedy, O. D., et al. 2012. Activation of resorption in fatigue-loaded bone involves both apoptosis and active pro-osteoclastogenic signaling by distinct osteocyte populations. *Bone* 50: 1115–1122.

Konieczynski, D. D., et al. 1998. Evaluation of a bone's *in vivo* 24-hour loading history for physical exercise compared with background loading. *J. Orthop. Res.* 16: 29–37.

Kupczik, K., et al. 2007. Assessing mechanical function of the zygomatic region in macaques: Validation and sensitivity testing of finite element models. *J. Anat.* 210: 41–53.

Lanyon, L. E. 1972. *In vivo* bone strain recorded from thoracic vertebrae of sheep. *J. Biomech.* 5: 277–281.

Lanyon, L. E. 1973. Analysis of surface bone strain in the calcaneus of sheep during normal locomotion. Strain analysis of the calcaneus. *J. Biomech.* 6: 41–49.

Lanyon, L. E. and S. Bourn. 1979. The influence of mechanical function on the development and remodeling of the tibia. *J. Bone Joint Surg. A* 61: 262–273.

Lanyon, L. E., et al. 1979. The relationship of functional stress and strain to the processes of bone remodelling. An experimental study on the sheep radius. *J. Biomech.* 12: 593–600.

Lanyon, L. E., et al. 1981. *In vivo* strain measurements from bone and prosthesis following total hip replacement. An experimental study in sheep. *J. Bone Joint Surg. A* 63: 989–1001.

Lauder, G. V. and L. E. Lanyon. 1980. Functional anatomy of feeding in the bluegill sunfish, *Lepomis macrochirus*: *In vivo* measurement of bone strain. *J. Exp. Biol.* 84: 33–55.

Ledogar, J. A., et al. 2016. Mechanical evidence that *Australopithecus sediba* was limited in its ability to eat hard foods. *Nat. Comm.* 7: 1–9.

Lee, K. C. L., et al. 2002. Validation of a technique for studying functional adaptation of the mouse ulna in response to mechanical loading. *Bone* 31: 1–9.

Lieberman, D. E., et al. 2004a. Effects of food processing on masticatory strain and craniofacial growth in a retrognathic face. *J. Human Evol.* 46: 655–677.

Lieberman, D. E., et al. 2004b. Predicting long bone loading from cross-sectional geometry. *Am. J. Phys. Anthropol.* 123: 156–171.

Liu, J., et al. 2012. The application of muscle wrapping to voxel-based finite element models of skeletal structures. *Biomech. Model. Mechanobiol.* 11: 35–47.

Loitz, B. J. and R. F. Zernicke. 1992. Strenuous exercise-induced remodelling of mature bone: Relationships between *in vivo* strains and bone mechanics. *J. Exp. Biol.* 170, 1–18.

Main, R. P. and A. A. Biewener. 2004. Ontogenetic patterns of limb loading, *in vivo* bone strains and growth in the goat radius. *J. Exp. Biol.* 207: 2577–2588.

Main, R. P. and A. A. Biewener. 2006. *In vivo* bone strain and ontogenetic growth patterns in relation to life-history strategies and performance in two vertebrate taxa: Goats and emu. *Physiol. Biochem. Zool.* 79: 57–72.

Main, R. P. and A. A. Biewener. 2007. Skeletal strain patterns and growth in the emu hindlimb during ontogeny. *J. Exp. Biol.* 210: 2676–2690.

Manafzadeh, A. R. and K. Padian. 2018. ROM mapping of ligamentous constraints on avian hip mobility: Implications for extinct ornithodirans. *Proc. R. Soc. B: Biol. Sci.* 285(1879): 20180727. https://doi.org/10.1098/rspb.2018.0727

Manley, P. A., et al. 1982. Evaluation of tension and compression forces in the canine femur *in vivo*. *Arch. Orthop. Trauma. Surg.* 99: 213–216.

Markey, M. J., et al. 2006. *In vivo* cranial suture function and suture morphology in the extant fish *Polypterus*: Implications for inferring skull function in living and fossil fish. *J. Exp. Biol.* 209: 2085–2102.

Martínez-Pérez, C., et al. 2014. Finite element, occlusal, microwear and microstructural analyses indicate that conodont microstructure is adapted to dental function. *Palaeontology* 57: 1059–1066.

McGowan, C. P., et al. 2005. The mechanics of jumping *versus* steady hopping in yellow-footed rock wallabies. *J. Exp. Biol.* 208: 2741–2751.

Mehta, S. S., et al. 1999. Bone material elasticity in a murine model of osteogenesis imperfecta. *Connect. Tissue Res.* 40: 189–198.

Metzger, K. A., et al. 2005. Comparison of beam theory and finite-element analysis with *in vivo* bone strain data from the alligator cranium. *Anat. Rec. A*283: 331–348.

Milgrom, C., et al. 2000. *In vivo* strain measurements to evaluate the strengthening potential of exercises on the tibial bone. *J. Bone Joint Surg. B* 82: 591–594.

Mirzaali, M. J., et al. 2016. Mechanical properties of cortical bone and their relationships with age, gender, composition and microindentation properties in the elderly. *Bone* 93: 196–211.

Moazen, M., et al. 2008a. Combined finite element and multibody dynamics analysis of biting in a *Uromastyx hardwickii* lizard skull. *J. Anat.* 213: 499–508.

Moazen, M., et al. 2008b. Rigid-body analysis of a lizard skull: Modelling the skull of *Uromastyx hardwickii*. *J. Biomech.* 41: 1274–1280.

Moreno, C. A., et al. 2008. Variability in forelimb bone strains during non-steady locomotor activities in goats. *J. Exp. Biol.* 211: 1148–1162.

Morgan, E. F., et al. 2018. Bone mechanical properties in healthy and diseased states. *Ann. Rev. Biomed. Eng.* 20: 119–143.

Mosley, J. R., et al. 1997. Strain magnitude related changes in whole bone architecture in growing rats. *Bone* 20: 191–198.

Nunamaker, D. M., et al. 1990. Fatigue fractures in thoroughbred racehorses: Relationships with age, peak bone strain, and training. *J. Orthop. Res.* 8: 604–611.

Nyakatura, J. A., et al. 2019. Reverse-engineering the locomotion of a stem amniote. *Nature* 565(7739): 351–355.

O'Higgins, P., et al. 2019. Geometric morphometrics and finite elements analysis: Assessing the functional implications of differences in craniofacial form in the hominin fossil record. *J Archaeol. Sci.* 101: 159–168.

O'Higgins, P., et al. 2012. Virtual functional morphology: Novel approaches to the study of craniofacial form and function. *Evol. Biol.* 39: 521–535.

Panagiotopoulou, O., et al. 2012. What makes an accurate and reliable subject-specific finite element model? A case study of an elephant femur. *J. R. Soc. Interface* 9: 351–361.

Panagiotopoulou, O., et al. 2017. *In vivo* bone strain and finite element modeling of a rhesus macaque mandible during mastication. *Zoology* 124: 13–29.

Peterson, J. and P. C. Dechow. 2003. Material properties of the human cranial vault and zygoma. *Anat. Rec. A*274: 785–797.

Pierce, S. E., et al. 2008. Patterns of morphospace occupation and mechanical performance in extant crocodilian skulls: A combined geometric morphometric and finite element modeling approach. *J. Morphol.* 269: 840–864.

Polly, P. D., et al. 2016. Combining geometric morphometrics and finite element analysis with evolutionary modeling: Towards a synthesis. *J. Vert. Paleontol.* 36(4): e1111225. https://doi.org/10.1080/02724634.2016.1111225

Porro, L. B., et al. 2013. *In vivo* bone strain and finite element modeling of the mandible of *Alligator mississippiensis*. *J. Anat.* 223: 195–227.

Porro, L. B., et al. 2014. *In vivo* cranial bone strain and bite force in the agamid lizard *Uromastyx geyri*. *J. Exp. Biol.* 217: 1983–1992.

Purnell, M. A. 1993. Feeding mechanisms in conodonts and the function of the earliest vertebrate hard tissues. *Geology* 21: 375–377.

Qiu, S., et al. 2002. Age and distance from the surface but not menopause reduce osteocyte density in human cancellous bone. *Bone* 31: 313–318.

Rabkin, B. A., et al. 2001. Long-term measurement of bone strain in vivo: The rat tibia. *J. Biomed. Mat. Res.* 58: 277–281.

Rafferty, K. L., et al. 2000. Three-dimensional loading and growth of the zygomatic arch. *J. Exp. Biol.* 203: 2093–2104.

Rankin, J. W., et al. 2018. Functional capacity of kangaroo rat hindlimbs: Adaptations for locomotor performance. *J. R. Soc. Interface* 15(144): 20180303. https://doi.org/10.1098/rsif.2018.0303

Ravosa, M. J., et al. 2000a. Masticatory stress, orbital orientation and the evolution of the primate postorbital bar. *J. Hum. Evol. 38*: 667–693.

Ravosa, M. J., et al. 2000b. Strain in the galago facial skull. *J. Morphol.* 245: 51–66.

Rayfield, E. J. 2007. Finite element analysis and understanding the biomechanics and evolution of living and fossil organisms. *Ann. Rev. Earth Planet. Sci.* 35: 541–576.

Reilly, D. T. and A. H. Burstein 1975. The elastic and ultimate properties of compact bone tissue. *J. Biomech. 8*: 393–405.

Reilly, S. M. and J. A. Elias. 1998. Locomotion in *Alligator mississippiensis*: Kinematic effects of speed and posture and their relevance to the sprawling-to-erect paradigm. *J. Exp. Biol*. 201: 2559–2574.

Reilly, D. T., et al. 1974. The elastic modulus for bone. *J. Biomech*. 7: 271–275.

Reilly, S. M., et al. 2005. Hindlimb function in the alligator: Integrating movements, motor patterns, ground reaction forces and bone strain of terrestrial locomotion. *J. Exp. Biol*. 208: 993–1009.

Rensberger, J. M. 1995. Determination of stresses in mammalian dental enamel and their relevance to the interpretation of feeding behaviors in extinct taxa. In *Functional morphology in vertebrate paleontology*, ed. Thomason J. J., 151–171. Cambridge, UK: Cambridge University Press.

Reumann, M. K., et al. 2011. Early growth response gene 1 regulates bone properties in mice. *Calcif. Tissue Int*. 89: 1–9.

Richards, C. T. and A. A. Biewener. 2007. Modulation of *in vivo* muscle power output during swimming in the African clawed frog (*Xenopus laevis*). *J. Exp. Biol*. 210: 3147–3159.

Ross, C. F. 2001. *In vivo* function of the craniofacial haft: The interorbital "pillar." *Am. J. Phys. Anthropol*. 116: 108–139.

Ross, C. F. and W. L. Hylander. 1996. *In vivo* and *in vitro* bone strain in the owl monkey circumorbital region and the function of the postorbital septum. *Am. J. Phys. Anthropol*. 101: 183–215.

Ross, C. F. and K. A. Metzger. 2004. Bone strain gradients and optimization in vertebrate skulls. *Ann. Anat*. 186: 387–396.

Ross, C. F., et al. 2005. Modeling masticatory muscle force in finite element analysis: Sensitivity analysis using principal coordinates analysis. *Anat. Rec. A*283: 288–299.

Ross, C. F., et al. 2016. *In vivo* bone strain in the mandibular corpus of *Sapajus* during a range of oral food processing behaviors. *J. Hum. Evol. 98*: 36–65.

Ross, C. F., et al. 2018. Bite force and cranial bone strain in four species of lizards. *J. Exp. Biol*. 221(Pt 23): jeb180240. https://doi.org/10.1242/jeb.180240

Rubin, C. T. and L. E. Lanyon. 1982. Limb mechanics as a function of speed and gait: A study of functional strains in the radius and tibia of horse and dog. *J. Exp. Biol*. 101: 187–211.

Rubin, C. T. and L. E. Lanyon. 1984a. Dynamic strain similarity in vertebrates; An alternative to allometric limb bone scaling. *J. Theor. Biol*. 107: 321–327.

Rubin, C. T. and L. E. Lanyon. 1984b. Regulation of bone formation by applied dynamic loads. *J. Bone Joint Surg. A* 66: 397–402.

Rubin, C. T. and L. E. Lanyon. 1985. Regulation of bone mass by mechanical strain magnitude. *Calcif. Tissue Int*. 37: 411–417.

Santana, S. E., et al. 2012. Dietary hardness, loading behavior, and the evolution of skull form in bats. *Evolution* 66: 2587–2598.

Sheffield, K. M. and R. W. Blob. 2011. Loading mechanics of the femur in tiger salamanders (*Ambystoma tigrinum*) during terrestrial locomotion. *J. Exp. Biol*. 214: 2603–2615.

Sheffield, K. M., et al. 2011. Locomotor loading mechanics in the hindlimbs of tegu lizards (*Tupinambis merianae*): Comparative and evolutionary implications. *J. Exp. Biol*. 214: 2616–2630.

Shi, J., et al. 2012. Developing a musculoskeletal model of the primate skull: Predicting muscle activations, bite force, and joint reaction forces using multibody dynamics analysis and advanced optimisation methods. *J. Theor. Biol*. 310: 21–30.

Smith, K. K. and W. L. Hylander, 1985. Strain gauge measurement of mesokinetic movement in the lizard *Varanus exanthematicus*. *J. Exp. Biol*. 114: 53–70.

Smith, A. L., et al. 2015a. Biomechanical implications of intraspecific shape variation in chimpanzee crania: Moving toward an integration of geometric morphometrics and finite element analysis. *Anat. Rec*. 298: 122–144.

Smith, A. L., et al. 2015b. The feeding biomechanics and dietary ecology of *Paranthropus boisei*. *Anat. Rec*. 298: 145–167.

Stansfield, E., et al. 2018a. A sensitivity study of human mandibular biting simulations using finite element analysis. *J. Archaeol. Sci. Rep*. 22: 420–432.

Stansfield, E., et al. 2018b. Can diet be inferred from the biomechanical response to simulated biting in modern and pre-historic human mandibles? *J. Archaeol. Sci.: Rep*. 22: 433–443.

Stein, K. W. H. and J. Werner. 2013. Preliminary analysis of osteocyte lacunar density in long bones of tetrapods: All measures are bigger in sauropod dinosaurs. *PLoS One*, 8: 1–9. https://doi.org/10.1371/journal.pone.0077109

Strait, D. S., et al. 2005. Modeling elastic properties in finite-element analysis: How much precision is needed to produce an accurate model? *Anat. Rec. A* 283: 275–287.

Strait, D. S., et al. 2009. The feeding biomechanics and dietary ecology of *Australopithecus africanus*. *Proc. Nat. Acad. Sci. U S A* 106: 2124–2129.

Sugiyama, T., et al. 2012. Bone's adaptive response to mechanical loading is essentially linear between the low strains associated with disuse and the high strains associated with the lamellar/woven bone transition. *J. Bone Miner. Res*. 27: 1784–1793.

Sun, Z., et al. 2004. Cranial sutures and bones: Growth and fusion in relation to masticatory strain. *Anat. Rec. A* 276: 150–161.

Swartz, S. M., et al. 1992. Wing bone stresses in free flying bats and the evolution of skeletal design for flight. *Nature* 359 (6397): 726–729.

Swartz, S. M., et al. 1989. Telemetered *in vivo* strain analysis of locomotor mechanics of brachiating gibbons. *Nature* 342(6247): 270–272.

Thomason, J. J., et al. 2001. *In vivo* surface strain and stereology of the frontal and maxillary bones of sheep: Implications for the structural design of the mammalian skull. *Anat. Rec*. 264: 325–338.

Tsai, H. P., et al. 2020. Contrast-enhanced XROMM reveals *in vivo* soft tissue interactions in the hip of *Alligator mississippiensis*. *J. Anat*. 236: 288–304.

van der Meulen, M. C. H., et al. 1993. Mechanobiologic influences in long-bone cross-sectional growth. *Bone* 14: 635–642.

van der Meulen, M. C. H., et al. 2001. Understanding bone strength: Size isn't everything. *Bone* 29: 101–104.

Vashishth, D., et al. 2001. Influence of nonenzymatic glycation on biomechanical properties of cortical bone. *Bone* 28: 195–201.

Verner, K. A., et al. 2016. Experimental tests of planar strain theory for predicting bone cross-sectional longitudinal and shear strains. *J. Exp. Biol*. 219: 3082–3090.

Wainwright, S. A., et al. 1982. *Mechanical design in organisms*. 2nd ed. Princeton, NJ, Princeton University Press.

Wang, Q. and P. C. Dechow. 2006. Elastic properties of external cortical bone in the craniofacial skeleton of the Rhesus monkey. *Am. J. Phys. Anthropol*. 131: 402–415.

Wang, Y., et al. 2008. Strain amplification and integrin based signaling in osteocytes. *J. Musculoskel. Neuronal Interact*. 8: 332–334.

Weijs, W. A. and H. J. de Jongh. 1977. Strain in mandibular alveolar bone during mastication in the rabbit. *Arch. Oral Biol*. 22: 667–675.

Witmer, L. M. 1995. The extant phylogenetic bracket and the importance of reconstructing soft tissues in fossils. In *Functional morphology in vertebrate paleontology*, ed. Thomason, J. J., 19–33. Cambridge, UK, Cambridge University Press.

Yang, H., et al. 2014. Characterization of cancellous and cortical bone strain in the *in vivo* mouse tibial loading model using micro-CT-based finite element analysis. *Bone* 66: 131–139.

Yang, H., et al. 2019. Adaptive changes in micromechanical environments of cancellous and cortical bone in response to *in vivo* loading and disuse. *J. Biomech*. 89: 85–94.

You, L., et al. 2001. A model for strain amplification in the actin cytoskeleton of osteocytes due to fluid drag on pericellular matrix. *J. Biomech*. 34: 1375–1386.

Young, V. K. H. and R. W. Blob. 2015. Limb bone loading in swimming turtles: Changes in loading facilitate transitions from tubular to flipper-shaped limbs during aquatic invasions. *Biol. Lett*. 11: 20150110. https://doi.org/10.1098/rsbl.2015.0110

Young, V. K. H., et al. 2017. Humeral loads during swimming and walking in turtles: Implications for morphological change during aquatic reinvasions. *J. Exp. Biol*. 220: 3873–3877.